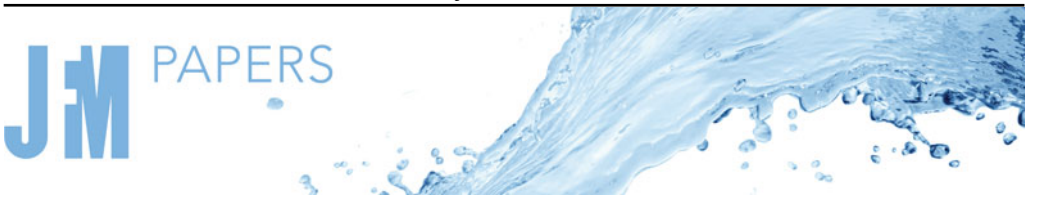
J. Fluid Mech. (2026), *vol.* 1040, A7, doi:10.1017/jfm.2026.11860



Singularity formation in electrified vortex sheets

Xin Guan[1] **and Demetrios T. Papageorgiou**[1]

[1]Department of Mathematics, Imperial College London, South Kensington Campus, London SW7 2AZ, UK

Corresponding author: Xin Guan, x.guan@imperial.ac.uk

(Received 20 April 2026 UTC; revised 3 June 2026 UTC; accepted 29 June 2026 UTC)

This study investigates the effect of a tangential electric field on the curvature singularity encountered by evolving vortex sheets. Weakly nonlinear models are derived by using asymptotic expansions based on the Dirichlet–Neumann operators. A fully nonlinear boundary integral method based on Cauchy's integral formula and an angle –arclength derivative formulation in a Lagrangian framework is proposed. Linear stability analysis reveals a transition from the unstable regime to a neutrally stable regime at a critical electric field strength. However, both weakly nonlinear models and fully nonlinear simulations suggest that the curvature singularity persists regardless of the value of the electric field strength. The analysis demonstrates that the singularity time obeys two different asymptotic rules. For subcritical values of the tangential electric field and small initial amplitudes, the singularity time scales with the logarithm of the inverse of the amplitude, and monotonically increases with the electric field strength. For supercritical values of the tangential electric field the singular time is asymptotically larger, follows an inverse power law with respect to the initial amplitude and reaches local maxima as the electric field strength varies. Fully nonlinear simulations of the underlying electrodynamic Euler equations confirm that the curvature singularity can be significantly delayed when the electric field strength takes some special values. In the limit of large electric field strengths the numerical simulations indicate that the time to singularity formation is proportional to the inverse square root of the electric field strength.

Key words: waves/free-surface flows, computational methods, nonlinear instability

1. Introduction

It is well known that vortex-sheet evolution is ill posed and develops a curvature singularity in finite time due to the Kelvin–Helmholtz (K–H) instability (Moore 1979; Caflisch

© The Author(s), 2026. Published by Cambridge University Press. This is an Open Access article, distributed under the terms of the Creative Commons Attribution licence (https://creativecommons.org/licenses/by/4.0/), which permits unrestricted re-use, distribution and reproduction, provided the original article is properly cited.

https://doi.org/10.1017/jfm.2026.11860 Published online by Cambridge University Press

& Orellana 1986, 1989; Krasny 1986*b*; Caflisch *et al.* 1990; Pullin & Shen 2023). Regularisations by using vortex blobs (Krasny 1986*a*), vortex layers (Baker & Shelley 1990) and surface tension (Hou *et al.* 1994, 1997) have been shown to mitigate or cut off the high-wavenumber K–H instability and remove the curvature singularity. However, there still exist unstable eigenmodes which can cause the interface to roll up. On the other hand, it is known that a tangential electric field (TEF) can stabilise fluid systems in various physical scenarios (Melcher & Schwarz Jr. 1968; Tilley *et al.* 2001; Papageorgiou 2019). The Rayleigh–Taylor instability can be suppressed by a sufficiently strong TEF, as shown by weakly nonlinear models (Barannyk *et al.* 2012, 2015) and direct numerical simulations of the Navier–Stokes equations (Cimpeanu *et al.* 2014; Yang *et al.* 2016; Anderson *et al.* 2017). Linear stability analysis shows that a strong TEF can suppress the K–H instability for all wavenumbers, thus distinguishing it from the other regularisations mentioned above. Grandison *et al.* (2012) showed that coupling TEFs with surface tension can suppress rupture of planar jets. These studies motivate the current investigation on the electrified vortex-sheet problem, given the surmise that the vortex sheet could become well posed and the curvature singularity eliminated. However, there exists limited numerical evidence that suggests that the latter may not be true. Kochurin & Zubarev (2018) and Kochurin (2019*a*,*b*) found curvature singularities in surface gravity-capillary waves even when there is a strong TEF. A reasonable explanation is that a sufficiently strong TEF makes the system almost non-dispersive. Therefore, for small-amplitude perturbations, the leading-order asymptotic model should be a quadratic nonlinear equation without linear dispersive terms, which is likely to develop a shock in finite time. To our knowledge, the regularity of electrified vortex sheets and their evolution is an open question. Of interest also is the recent study by Sohn & Baek (2026) who address electrified vortex-sheet evolution by incorporating a vortex blob regularisation; hence, there is little overlap with our study which is entirely focussed on singularity formation and how it is affected by the electric field.

We consider vortex sheets between two dielectric, incompressible and inviscid fluids subjected to a uniform TEF. Given small-amplitude initial perturbations, we study their temporal evolution. To derive weakly nonlinear models, we take advantage of the Hamiltonian structure supported by the electrified vortex-sheet system. The Hamiltonian formulation was introduced to water waves by the pioneering work of Zakharov (1968). Later, Benjamin & Bridges (1997) extended this formulation to two-layer interfacial flows with a uniform background shear, i.e. the vortex-sheet problem. Recently, the Hamiltonian approach has been widely applied to studies of electrified surface and interfacial waves (Kochurin *et al.* 2013; Kochurin & Zubarev 2018; Wang 2017; Kochurin 2019*a*,*b*; Guan & Wang 2022; Wang 2022; Sohn & Baek 2026). In particular, Wang (2022) showed that the Hamiltonian of electrified two-layer shear-free potential flows is the Benjamin–Bridges Hamiltonian but incorporating the perturbed electric potential energy. By taking a variational derivative, the electric-energy term gives rise to the Maxwell stress tensor and leads to the correct dynamic boundary conditions. Combining the results of Benjamin & Bridges (1997) and Wang (2022), it is trivial to extend the Hamiltonian formulation to our current problem. The superiority of the Hamiltonian approach comes from the fact that the global dependence of the unknowns, i.e. the Birkhoff–Rott equation and its equivalent integral relations, is intrinsically built into the Dirichlet–Neumann operators (DNOs), which can be asymptotically truncated to arbitrary orders through the Craig–Sulem recursion relation (Craig & Sulem 1993). This property has been widely used to derive weakly nonlinear models in various physical scenarios (Craig & Groves 1994; Craig *et al.* 2012; Wang & Milewski 2012; Wang 2017; Guan & Wang 2022; Xu & Wang 2025; Feng & Yang 2026).

https://doi.org/10.1017/jfm.2026.11860 Published online by Cambridge University Press

For fully nonlinear simulations of vortex sheets, the most efficient approach is the boundary integral method (BIM). In two dimensions there are three often-used versions: by using the Birkhoff–Rott equation (Baker *et al.* 1982; Hou *et al.* 1994, 1997; Baker & Nachbin 1998; Ambrose *et al.* 2022); using a Green's function to derive a boundary integral equation (Longuet-Higgins & Cokelet 1976; Baker *et al.* 1982; Yang 1992); and deriving the boundary integral equation by using Cauchy's integral formula (Dold & Peregrine 1986; Dold 1992; Grue *et al.* 1997; Ambrose *et al.* 2022; Guan & Vanden-Broeck 2025). In this paper, we adopt the latter approach. Owing to the irrotationality and incompressibility of the flow field and the harmonic nature of the electrostatic field, one can introduce two related analytic functions that satisfy Cauchy's integral formula at the interface. The resulting boundary integral equations take the form of Fredholm integral equations of the second kind, enabling efficient implementation of iterative solvers such as the generalised minimum residual method (GMRES). To track the evolution of the interface, we employ the $\theta - s_\alpha$ formulation (Yang 1992; Hou *et al.* 1994; Guan & Vanden-Broeck 2025), which uses the tangent angle and the arclength derivative along the interface as primary unknowns. This removes the restriction that the interface must be a graph of the horizontal variable, allowing us to simulate overturned interfaces as long as there is no topological change. The formulation can be embedded into an Eulerian framework where all grid points are evenly separated using arclength as a parameter (Yang 1992; Hou *et al.* 1994; Guan & Vanden-Broeck 2025). By using the small-scale decomposition method (Hou *et al.* 1994, 1997) (essentially an integrating-factor technique), we can significantly eliminate the capillary-induced numerical stiffness. In the current paper, there is no severe numerical-stiffness issue because we do not consider surface tension. In contrast, we find that the Lagrangian approach provides superior computational accuracy because fluid markers can cluster in the region where the curvature singularity develops.

The rest of the paper is organised as follows. Section 2 describes the problem setting, mathematical formulation, non-dimensionalisation and linear dispersion relation. Section 3 illustrates the Hamiltonian formulation, expansions of the DNOs and derives various weakly nonlinear models, a special case of which is a novel evolution equation for classical vortex sheets. Section 4 demonstrates the BIM $\theta - s_\alpha$ formulation, and includes details of the fully nonlinear simulations. Section 5 reports numerical results of the BIM and compares them with solutions of the models. Section 6 provides our conclusions.

2. Governing equations

We consider an electrified vortex sheet between two immiscible ideal fluids with a uniform TEF of strength E_0 acting parallel to the initially flat interface. Inside each fluid, there is a constant background flow $\tilde{U}_j$, where the subscript j is used to denote the lower fluid when $j = 1$, and the upper fluid when $j = 2$. The fluids are assumed to be perfect dielectrics with constant permittivities ε_j and constant densities ρ_j. We use x and y to denote the usual horizontal and vertical Cartesian coordinates. For convenience, the y-axis points upwards and the x-axis points in the direction of the electric field and coincides with the undisturbed interface. A schematic is given in figure 1. If at some given time t the interface has elevation $\eta(x, t)$, our objective is to calculate the subsequent evolution of the interface and in particular investigate whether an initially smooth interface remains smooth at later times.

Assuming the flows are irrotational, we can introduce two perturbed velocity potentials ϕ_j so that the velocity $\boldsymbol{u}_j$ in each layer can be written as

$$\boldsymbol{u}_j = \tilde{U}_j \boldsymbol{i} + \nabla \phi_j, \quad \text{for} \quad j = 1 \quad \text{and} \quad 2, \tag{2.1}$$

https://doi.org/10.1017/jfm.2026.11860 Published online by Cambridge University Press

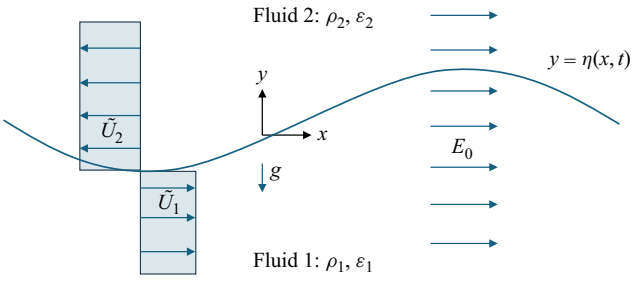


Figure 1. Schematic of the electrified vortex sheet.

where $\boldsymbol{i}$ denotes the unit vector in the x-direction, and $\nabla = (\partial_x, \partial_y)$. Similarly, the electrostatic limit of Maxwell's equations allows us to introduce perturbed voltage potentials V_1 and V_2 so that the electric field can be expressed as

$$\boldsymbol{E}_j = E_0\boldsymbol{i} + \nabla V_j, \quad \text{for} \quad j = 1 \quad \text{and} \quad 2. \tag{2.2}$$

The velocity and voltage potentials satisfy Laplace's equation

$$\begin{cases} \phi_{1,xx} + \phi_{1,yy} = 0, & \text{for} \quad -\infty < y < \eta(x,t), \\ V_{1,xx} + V_{1,yy} = 0, & \text{for} \quad -\infty < y < \eta(x,t), \\ \phi_{2,xx} + \phi_{2,yy} = 0, & \text{for} \quad \eta(x,t) < y < \infty, \\ V_{2,xx} + V_{2,yy} = 0, & \text{for} \quad \eta(x,t) < y < \infty. \end{cases} \tag{2.3}$$

At the interface $y = \eta(x,t)$, we have two kinematic boundary conditions

$$\begin{cases} \eta_t + (\tilde{U}_1 + \phi_{1,x})\eta_x = \phi_{1,y}, \\ \eta_t + (\tilde{U}_2 + \phi_{2,x})\eta_x = \phi_{2,y}, \end{cases} \tag{2.4}$$

and a dynamic boundary condition

$$\rho_1\left(\phi_{1,t} + \frac{1}{2}|\boldsymbol{u_1}|^2 + g\eta\right) - \rho_2\left(\phi_{2,t} + \frac{1}{2}|\boldsymbol{u_2}|^2 + g\eta\right) + \left[\boldsymbol{n}\cdot\boldsymbol{\Sigma}\cdot\boldsymbol{n}\right]_2^1 = 0, \tag{2.5}$$

where $\boldsymbol{n} = (-\eta_x, 1)/\sqrt{1+\eta_x^2}$ is the unit normal vector pointing into fluid 2, and $\boldsymbol{\Sigma}$ represents the Maxwell stress tensor

$$\boldsymbol{\Sigma} = \varepsilon_j \boldsymbol{E}_j \otimes \boldsymbol{E}_j - \frac{\varepsilon_j}{2}|\boldsymbol{E}_j|^2 I \qquad \text{in fluid } j. \tag{2.6}$$

After some algebra we can write

$$\left[\boldsymbol{n}\cdot\boldsymbol{\Sigma}\cdot\boldsymbol{n}\right]_2^1 = \frac{\varepsilon_1}{2}\left[\left(\boldsymbol{E}_1\cdot\boldsymbol{n}\right)^2 - \left(\boldsymbol{E}_1\cdot\boldsymbol{t}\right)^2\right] - \frac{\varepsilon_2}{2}\left[\left(\boldsymbol{E}_2\cdot\boldsymbol{n}\right)^2 - \left(\boldsymbol{E}_2\cdot\boldsymbol{t}\right)^2\right], \tag{2.7}$$

where $\boldsymbol{t} = (1, \eta_x)/\sqrt{1+\eta_x^2}$ is the unit tangent vector along the interface. In addition

$$\boldsymbol{E}_j\cdot\boldsymbol{n} = \frac{\partial V_j}{\partial \boldsymbol{n}} - E_0\frac{\eta_x}{\sqrt{1+\eta_x^2}}, \qquad \boldsymbol{E}_j\cdot\boldsymbol{t} = \frac{\partial V_j}{\partial \boldsymbol{t}} + E_0\frac{1}{\sqrt{1+\eta_x^2}}. \tag{2.8}$$

The notation $\partial V_j/\partial\boldsymbol{n} = \nabla V_j\cdot\boldsymbol{n}$ and $\partial V_i/\partial\boldsymbol{t} = \nabla V_j\cdot\boldsymbol{t}$ has been introduced in (2.8), and will be used in the remainder of the paper. Furthermore, we have two boundary conditions at $y = \eta(x,t)$ for the voltage potentials. Namely, continuity of voltage potentials

$$V_1 = V_2, \tag{2.9}$$

https://doi.org/10.1017/jfm.2026.11860 Published online by Cambridge University Press

and continuity of the electric displacement field

$$\varepsilon_1 \boldsymbol{E_1}\cdot\boldsymbol{n} - \varepsilon_2 \boldsymbol{E_1}\cdot\boldsymbol{n} = 0 \quad \Rightarrow \quad \varepsilon_1 \frac{\partial V_1}{\partial \boldsymbol{n}} - \varepsilon_2 \frac{\partial V_2}{\partial \boldsymbol{n}} = E_0(\varepsilon_1 - \varepsilon_2)\frac{\eta_x}{\sqrt{1+\eta_x^2}}. \tag{2.10}$$

Finally, we impose far-field conditions as $|y| \to \infty$

$$\phi_j \to 0, \quad V_j \to 0 \quad \text{for} \quad j = 1 \quad \text{and} \quad 2. \tag{2.11}$$

Without loss of generality we assume that $\tilde{U}_1 = -\tilde{U}_2 = \tilde{U}/2$ (a Galilean transformation can always achieve this). The system is non-dimensionalised by choosing typical scales for length, time, velocity, density, permittivity and electric field strength as

$$\frac{L}{2\pi}, \quad \frac{L}{2\pi|\tilde{U}|}, \quad |\tilde{U}|, \quad \rho_1, \quad \varepsilon_1, \quad E_0, \tag{2.12}$$

where L is the smallest spatial period of the initial periodic perturbation. The following dimensionless parameters emerge:

$$R = \frac{\rho_2}{\rho_1}, \quad F_r = \frac{|\tilde{U}|}{\sqrt{gL}}, \quad \varepsilon = \frac{\varepsilon_2}{\varepsilon_1}, \quad E_b = \frac{E_0^2\varepsilon_1}{\rho_1\tilde{U}^2}, \tag{2.13}$$

which denote the density ratio, the Froude number for the flow, the permittivity ratio and an electric Weber number that measures the strength of the imposed electric field. The dimensionless kinematic and dynamic boundary conditions now read

$$\begin{cases} \eta_t + \dfrac{U}{2}\eta_x + \phi_{1,x}\eta_x = \phi_{1,y}, \\ \eta_t - \dfrac{U}{2}\eta_x + \phi_{2,x}\eta_x = \phi_{2,y}, \\ \phi_{1,t} - R\phi_{2,t} + \dfrac{U}{2}(\phi_{1,x} + R\phi_{2,x}) + \dfrac{|\nabla\phi_1|^2}{2} - \dfrac{R|\nabla\phi_2|^2}{2} + \dfrac{(1-R)\eta}{F_r^2} + \dfrac{E_b}{2}\left[\boldsymbol{n}\cdot\boldsymbol{\Sigma}\cdot\boldsymbol{n}\right]_2^1 = 0, \end{cases} \tag{2.14}$$

where the dimensionless background shear U takes the values 1 or -1. The normal Maxwell shear stress (2.7) becomes

$$\begin{aligned} \left[\boldsymbol{n}\cdot\boldsymbol{\Sigma}\cdot\boldsymbol{n}\right]_2^1 = &\left[\frac{\partial V_1}{\partial \boldsymbol{n}} - \frac{\eta_x}{\sqrt{1+\eta_x^2}}\right]^2 - \left[\frac{\partial V_1}{\partial \boldsymbol{t}} + \frac{1}{\sqrt{1+\eta_x^2}}\right]^2 \\ &- \varepsilon\left[\frac{\partial V_2}{\partial \boldsymbol{n}} - \frac{\eta_x}{\sqrt{1+\eta_x^2}}\right]^2 + \varepsilon\left[\frac{\partial V_2}{\partial \boldsymbol{t}} + \frac{1}{\sqrt{1+\eta_x^2}}\right]^2, \end{aligned} \tag{2.15}$$

while the boundary conditions (2.9) and (2.10) become

$$\begin{cases} V_1 = V_2, \\ \dfrac{\partial V_1}{\partial \boldsymbol{n}} - \varepsilon\dfrac{\partial V_2}{\partial \boldsymbol{n}} = (1-\varepsilon)\dfrac{\eta_x}{\sqrt{1+\eta_x^2}}. \end{cases} \tag{2.16}$$

Solving the linearised system by looking for solutions proportional to $\mathrm{e}^{i(kx-\omega t)}$ (see Appendix A, where we also include a physical discussion of the stabilising electrostatic

https://doi.org/10.1017/jfm.2026.11860 Published online by Cambridge University Press

mechanism), one can derive two branches for the dispersion relation, namely

$$\omega = \frac{U(1-R)}{2(1+R)}k \pm \sqrt{\frac{1-R}{(1+R)F_r^2}|k| + \frac{E_b(1-\varepsilon)^2}{(1+\varepsilon)(1+R)}k^2 - \frac{R}{(1+R)^2}k^2}. \tag{2.17}$$

The three terms inside the square root represent, from left to right, the effects of buoyancy, the TEF and the background shear, respectively. When $R \leqslant 1$ (i.e. the heavier fluid is below), the system is neutrally stable for sufficiently strong fields satisfying

$$E_b > \frac{R(1+\varepsilon)}{(1+R)(1-\varepsilon)^2}. \tag{2.18}$$

Otherwise, it is linearly unstable due to the K–H instability. Note also that if Rayleigh–Taylor instability enters when $R > 1$, then the flow will be linearly unstable for long enough waves (small enough k) irrespective of the value of E_b. The interplay between Rayleigh–Taylor instability and the electric field has been considered for both inviscid and viscous flows (Barannyk *et al.* 2012, 2015; Cimpeanu *et al.* 2014; Yang *et al.* 2016; Guo *et al.* 2023).

Physically, the insulating perfect dielectric fluids modelled here will support polarisation charges on the interface. Following Jackson (2012, pp. 108–112), the polarisation-charge density is given by

$$\sigma_p = (\boldsymbol{P}_1 - \boldsymbol{P}_2)\cdot\boldsymbol{n}, \tag{2.19}$$

where $\boldsymbol{P}_{1,2}$ are polarisations defined by (in dimensional form)

$$\boldsymbol{P}_{1,2} = \frac{1}{4\pi}\left(\frac{\varepsilon_{1,2}}{\varepsilon_0} - 1\right)\boldsymbol{E}_{1,2}, \tag{2.20}$$

with ε_0 being the electric permittivity of free space. After simplification, we have

$$\sigma_p = \frac{\varepsilon_1 \boldsymbol{E_1}\cdot\boldsymbol{n} - \varepsilon_2 \boldsymbol{E_2}\cdot\boldsymbol{n}}{4\pi\varepsilon_0} + \frac{\boldsymbol{E_1}\cdot\boldsymbol{n} - \boldsymbol{E_2}\cdot\boldsymbol{n}}{4\pi}. \tag{2.21}$$

Using (2.8) and (2.10) gives the desired polarisation-charge distribution on the sheet

$$\sigma_p = \frac{1}{4\pi}\left(\frac{\partial V_1}{\partial \boldsymbol{n}} - \frac{\partial V_2}{\partial \boldsymbol{n}}\right). \tag{2.22}$$

3. Weakly nonlinear models

Zakharov (1968) first demonstrated that the water-wave problem under incompressible, irrotational and inviscid assumptions has a Hamiltonian structure. Later, Benjamin & Bridges (1997) extended the Hamiltonian formulation to two-layer potential flows with a uniform background shear at the interface. They showed that the Hamiltonian is the perturbed energy of the system, and the two canonical variables are the interface elevation η and the combination of the two perturbed velocity potentials $\varphi = \varphi_1 - R\varphi_2$, where $\varphi_1 = \phi_1(x, \eta, t)$ and $\varphi_2 = \phi_2(x, \eta, t)$. More recently, the Hamiltonian approach has been widely applied to studies of electrified surface and interfacial waves (Kochurin *et al.* 2013; Kochurin & Zubarev 2018; Wang 2017; Kochurin 2019*a*,*b*; Guan & Wang 2022; Wang 2022). In particular, Wang (2022) showed that the Hamiltonian of the electrified two-layer interfacial wave problem, is the Benjamin–Bridges Hamiltonian incorporating the perturbed electric potential energy. Although Wang's analysis does not account for the presence of background shear, we have confirmed that the conclusions remain valid for the present electrified vortex-sheet problem. This is evident since the variational derivative

https://doi.org/10.1017/jfm.2026.11860 Published online by Cambridge University Press

of the electrical potential energy only modifies the canonical equation of φ, i.e. the dynamic boundary condition, and gives rise to the Maxwell stress term. Incorporating the work of Benjamin and Bridges and that of Wang, an alternative formulation of the electrified vortex-sheet problem considered here is

$$\eta_t = \frac{\delta \mathcal{H}}{\delta \varphi}, \quad \varphi_t = -\frac{\delta \mathcal{H}}{\delta \eta}, \tag{3.1}$$

where the Hamiltonian $\mathcal{H}$ reads

$$\mathcal{H} = \underbrace{\frac{1}{2}\int_{-\infty}^{\eta}\int_0^{2\pi}\left(|\boldsymbol{u}_1|^2 - \frac{1}{4}\right)\mathrm{d}x\mathrm{d}y + \frac{R}{2}\int_{\eta}^{\infty}\int_0^{2\pi}\left(|\boldsymbol{u}_2|^2 - \frac{1}{4}\right)\mathrm{d}x\mathrm{d}y}_{\text{kinetic energy}} + \underbrace{\frac{1-R}{2F_r^2}\int_0^{2\pi}\eta^2\,\mathrm{d}x}_{\text{gravitational energy}}$$
$$+ \underbrace{\frac{E_b}{2}\int_{-\infty}^{\eta}\int_0^{2\pi}|\nabla V_1|^2\,\mathrm{d}x\mathrm{d}y + \frac{E_b\varepsilon}{2}\int_{\eta}^{\infty}\int_0^{2\pi}|\nabla V_2|^2\,\mathrm{d}x\mathrm{d}y}_{\text{electric energy}}. \tag{3.2}$$

To derive weakly nonlinear models, we introduce DNOs, which map the Dirichlet boundary condition of Laplace's equation to the corresponding Neumann boundary condition. For our two-layer fluid system, the DNOs $G^{\pm}(\eta)$ are defined by

$$\begin{cases} G^-(\eta)\varphi_1 = \dfrac{\partial \phi_1}{\partial \boldsymbol{n}}\sqrt{1+\eta_x^2}, \quad G^+(\eta)\varphi_2 = -\dfrac{\partial \phi_2}{\partial \boldsymbol{n}}\sqrt{1+\eta_x^2}, \\ G^-(\eta)V = \dfrac{\partial V_1}{\partial \boldsymbol{n}}\sqrt{1+\eta_x^2}, \quad G^+(\eta)V = -\dfrac{\partial V_2}{\partial \boldsymbol{n}}\sqrt{1+\eta_x^2}, \end{cases} \tag{3.3}$$

where

$$V = V_1(x,\eta,t) = V_2(x,\eta,t), \tag{3.4}$$

with the last condition following from (2.9). Using the divergence theorem, $\mathcal{H}$ can be rewritten as

$$\mathcal{H} = \frac{1}{2}\int_0^{2\pi}\left(\varphi_1 G^-(\eta)\varphi_1 + R\varphi_2 G^+(\eta)\varphi_2\right)\mathrm{d}x - \frac{U}{2}\int_0^{2\pi}(\varphi_1 + R\varphi_2)\eta_x\,\mathrm{d}x$$
$$+ \frac{1-R}{2F_r^2}\int_0^{2\pi}\eta^2\,\mathrm{d}x + \frac{E_b}{2}\int_0^{2\pi}\left(VG^-(\eta)V + \varepsilon VG^+(\eta)V\right)\mathrm{d}x. \tag{3.5}$$

After further simplifications (see Appendix B), we arrive at

$$\mathcal{H} = \frac{1}{2}\int \varphi G^-(G^+ + RG^-)^{-1}G^+\varphi\,\mathrm{d}x - \frac{U}{2}\int \eta_x(G^+ + RG^-)^{-1}(G^+ - RG^-)\varphi\,\mathrm{d}x$$
$$- \frac{R}{2}\int \eta_x(G^+ + RG^-)^{-1}\eta_x\,\mathrm{d}x + \frac{1-R}{2F_r^2}\int \eta^2\,\mathrm{d}x + \frac{E_b(1-\varepsilon)^2}{2}\int \eta_x(G^- + \varepsilon G^+)^{-1}\eta_x\,\mathrm{d}x, \tag{3.6}$$

where for brevity we have dropped the lower and upper limits of integration, and the dependence of $G^{\pm}$ on η. Combining the DNOs and (2.16) leads to the form of the voltage potential

$$V = (1-\varepsilon)(G^- + \varepsilon G^+)^{-1}\eta_x. \tag{3.7}$$

https://doi.org/10.1017/jfm.2026.11860 Published online by Cambridge University Press

Assuming $\eta = O(\delta)$ where $\delta \ll 1$, the DNOs have convergent Taylor series (Coifman & Meyer 1985)

$$G^- = \sum_{n=0}^{\infty} G_n, \quad G^+ = \sum_{n=0}^{\infty} (-1)^n G_n, \tag{3.8}$$

where $G_n = O(\delta^n)$. To derive a quadratic nonlinear model we only need the first two terms in the expansions, and these can be explicitly written down by using the Craig–Sulem expansion (Craig & Sulem 1993)

$$G_0 = (-\partial_{xx})^{1/2}, \tag{3.9}$$

$$G_1 = -G_0 \eta G_0 - \partial_x \eta \partial_x. \tag{3.10}$$

The composite operators in (3.6) can be asymptotically expanded using G_0 and G_1. For consistency with linear theory, we further assume that $\varphi = O(\delta)$. Thus, an approximate Hamiltonian $\mathcal{H}_3$, truncated to $O(\delta^3)$, reads

$$\begin{aligned}\mathcal{H}_3 =& \frac{1}{2(1+R)} \int \varphi G_0 \varphi \,\mathrm{d}x + \frac{B}{2} \int \eta_x G_0^{-1} \eta_x \,\mathrm{d}x - C \int \eta_x \varphi \,\mathrm{d}x + \frac{1-R}{2F_r^2} \int \eta^2 \,\mathrm{d}x \\ & - \frac{A}{2(1+R)} \int \left(\varphi G_0 \eta G_0 \varphi + \varphi \partial_x \eta \partial_x \varphi\right) \mathrm{d}x + \frac{D}{2} \int \left(\eta_x G_0^{-1} \partial_x \eta \partial_x G_0^{-1} \eta_x + \eta \eta_x^2\right) \mathrm{d}x \\ & + \left(AC - \frac{U}{2}\right) \int \left(\eta_x G_0^{-1} \partial_x \eta \partial_x \varphi + \eta \eta_x G_0 \varphi\right) \mathrm{d}x,\end{aligned} \tag{3.11}$$

where

$$\begin{aligned} A &= \frac{1-R}{1+R}, \quad B = \frac{E_b(1-\varepsilon)^2}{1+\varepsilon} - \frac{R}{1+R}, \\ C &= \frac{U(1-R)}{2(1+R)}, \quad D = \frac{E_b(1-\varepsilon)^3}{(1+\varepsilon)^2} + \frac{R(1-R)}{(1+R)^2}. \end{aligned} \tag{3.12}$$

Setting $R = 1$ and using (3.1) lead to the following weakly nonlinear model, correct to $O(\delta^2)$,

$$\begin{cases} \eta_t = -\dfrac{1}{2}\mathrm{H}[\varphi_x] - \dfrac{U}{2}\left(\left(\eta \mathrm{H}[\eta_x]\right)_x - \mathrm{H}[\eta\eta_x]_x\right), \\ \varphi_t = \left(\dfrac{E_b(1-\varepsilon)^2}{1+\varepsilon} - \dfrac{1}{2}\right)\mathrm{H}[\eta_x] + \dfrac{E_b(1-\varepsilon)^3}{2(1+\varepsilon)^2}\left(2\mathrm{H}\left[\eta \mathrm{H}[\eta_x]\right]_x + \mathrm{H}[\eta_x]^2 - \eta_x^2 + 2(\eta\eta_x)_x\right) \\ \quad - \dfrac{U}{2}\left(\mathrm{H}[\eta\varphi_x]_x + \varphi_x \mathrm{H}[\eta_x] + \eta_x \mathrm{H}[\varphi_x] - \left(\eta \mathrm{H}[\varphi_x]\right)_x\right), \end{cases} \tag{3.13}$$

where H is the Hilbert transform defined by

$$\mathrm{H}[f](x) = \frac{1}{\pi} \fint_{-\infty}^{\infty} \frac{f(x')}{x' - x} \,\mathrm{d}x'. \tag{3.14}$$

In Fourier space, $\widehat{\mathrm{H}} = \mathrm{i}\,\mathrm{sgn}(k)$. The corresponding approximation of the voltage potential (again correct to $O(\delta^2)$) is

$$V = \frac{1-\varepsilon}{1+\varepsilon}\mathrm{H}[\eta] + \frac{(1-\varepsilon)^2}{(1+\varepsilon)^2}\left(\eta\eta_x + \mathrm{H}\left[\eta \mathrm{H}[\eta_x]\right]\right). \tag{3.15}$$

https://doi.org/10.1017/jfm.2026.11860 Published online by Cambridge University Press

For stability, a critical electric field strength E_b^c follows from the linearised forms of (3.13)

$$E_b^c = \frac{1+\varepsilon}{2(1-\varepsilon)^2}. \tag{3.16}$$

This value aligns with (2.18), as expected. In what follows we consider the evolution of the vortex sheet subject to subcritical ($E_b < E_b^c$) and supercritical ($E_b > E_b^c$) electric fields.

For completeness, we derive the asymptotic form of the polarisation-charge density σ_p given by (2.22). Using the definitions (3.3) along with the interfacial voltage potential (3.7), allows us to express

$$\sigma_p = \frac{1}{4\pi}\left(\frac{\partial V_1}{\partial \boldsymbol{n}} - \frac{\partial V_2}{\partial \boldsymbol{n}}\right) = \frac{1-\varepsilon}{4\pi\sqrt{1+\eta_x^2}}(G^- + G^+)(G^- + \varepsilon G^+)^{-1}\eta_x. \tag{3.17}$$

At leading order, $G^{\pm} \sim G_0$ – see (3.8), thus

$$\sigma_p \sim \frac{1-\varepsilon}{2\pi(1+\varepsilon)}\frac{\eta_x}{\sqrt{1+\eta_x^2}}. \tag{3.18}$$

It is shown later that a finite-time curvature singularity forms at some point, implying that σ_p has a cusp in its spatial distribution. This has been confirmed by results of the model and the full Euler problem (for brevity the results are not included here).

3.1. *Subcritical tangential electric field, $E_b < E_b^c$.*

Following Kochurin *et al.* (2013) and Gao *et al.* (2024), we introduce two auxiliary functions

$$p = \frac{\varphi + 2\lambda\eta}{2}, \quad q = \frac{\varphi - 2\lambda\eta}{2}, \tag{3.19}$$

where

$$\lambda = \sqrt{\frac{1}{4} - \frac{E_b(1-\varepsilon)^2}{2(1+\varepsilon)}}. \tag{3.20}$$

The choice of λ follows from (2.17) with $R = 1$ that gives the growth rate to be $\omega = \pm\lambda k$ in the subcritical case. Note that p and q correspond to the exponentially growing and decaying eigenmodes of the linearised system. To simplify the model, we assume that the initial condition only contains a linearly growing mode. Therefore, it is reasonable to assume $q = o(\delta^2)$ and thus omit all nonlinear terms involving q. Equations (3.13) then become

$$p_t - q_t = -\lambda \mathrm{H}[p_x] - \lambda \mathrm{H}[q_x] - \frac{U}{4\lambda}\big((p\mathrm{H}[p_x])_x - \mathrm{H}[pp_x]_x\big), \tag{3.21}$$

$$\begin{aligned} p_t + q_t = &-\lambda \mathrm{H}[p_x] + \lambda \mathrm{H}[q_x] + \frac{E_b(1-\varepsilon)^3}{8\lambda^2(1+\varepsilon)^2}\big(2\mathrm{H}\big[p\mathrm{H}[p_x]\big]_x + \mathrm{H}[p_x]^2 - p_x^2 + 2(pp_x)_x\big) \\ &- \frac{U}{4\lambda}\big(\mathrm{H}[pp_x]_x + 2p_x\mathrm{H}[p_x] - \big(p\mathrm{H}[p_x]\big)_x\big). \end{aligned} \tag{3.22}$$

Adding (3.21) to (3.22) eliminates q_t to give

$$p_t + \lambda \mathrm{H}[p_x] = -\frac{U}{4\lambda}p_x\mathrm{H}[p_x] + \frac{E_b(1-\varepsilon)^3}{16\lambda^2(1+\varepsilon)^2}\big(2\mathrm{H}\big[p\mathrm{H}[p_x]\big]_x + \mathrm{H}[p_x]^2 + p_x^2 + 2pp_{xx}\big). \tag{3.23}$$

https://doi.org/10.1017/jfm.2026.11860 Published online by Cambridge University Press

An alternative equation for η is

$$\eta_t + \lambda \mathrm{H}[\eta_x] = -\frac{U}{2}\eta_x \mathrm{H}[\eta_x] + \frac{E_b(1-\varepsilon)^3}{8\lambda(1+\varepsilon)^2}\big(2\mathrm{H}\big[\eta \mathrm{H}[\eta_x]\big]_x + \mathrm{H}[\eta_x]^2 + \eta_x^2 + 2\eta\eta_{xx}\big), \tag{3.24}$$

where we have used the relation $p = 2\lambda\eta + o(\delta^2)$ that follows from (3.19). Note that prescribing the initial condition

$$\eta(x, 0) = \delta \sin(x), \tag{3.25}$$

to (3.24) is equivalent to giving initial condition

$$\eta(x, 0) = \delta \sin(x), \quad \varphi(x, 0) = 2\delta\lambda \sin(x), \tag{3.26}$$

to (3.13).

When $E_b = 0$, we obtain a quadratic nonlinear model for the classical vortex-sheet problem

$$\eta_t + \frac{1}{2}\mathrm{H}[\eta_x] + \frac{U}{2}\eta_x \mathrm{H}[\eta_x] = 0. \tag{3.27}$$

Equation (3.27) differs from the one derived and studied by Caflisch & Semmes (1990). To the best of our knowledge, (3.27) is a new vortex-sheet evolution model that has not been derived or studied previously in the literature. Note that (3.27) has similar features to the Constantin–Lax–Majda equation (Constantin *et al.* 1985), which is known to blow up in finite time. For (3.27), one can also derive the exact singularity formation time t_s by noting that it is equivalent to the following complex Burgers' equation (set $U = 1$ by rescaling):

$$W_t + \frac{\mathrm{i}}{2}(1 + W)W_x = 0, \tag{3.28}$$

where $W = \eta_x - \mathrm{i}\mathrm{H}[\eta_x]$. To trace the singularity, we solve (3.28) in the complex x-plane by using the method of characteristics. For the initial condition $W(x, 0) = \delta \mathrm{e}^{\mathrm{i}x}$ (consistent with (3.25)), the solution is written implicitly as

$$W = \delta \mathrm{e}^{\mathrm{i}\xi}, \quad \xi = x - \frac{\mathrm{i}}{2}\big(1 + \delta \mathrm{e}^{\mathrm{i}\xi}\big)t, \tag{3.29}$$

where $\xi \in \mathbb{C}$ labels different characteristics. The singularity first forms on $\xi = \xi^*$ where $x_\xi = 0$, leading to

$$\xi^* = 2\pi n + \mathrm{i} \ln \frac{\delta t}{2}, \tag{3.30}$$

where $n \in \mathbb{Z}$. The moment when the singularity intersects the real axis of the complex x-plane corresponds to the physical singularity time t_s, which gives

$$1 + \frac{t_s}{2} + \ln t_s = \ln \frac{2}{\delta}. \tag{3.31}$$

Replacing δ by $\delta/2$ (see the explanation below) gives the same result that Moore derived using the Birkhoff–Rott equation (Moore 1979). It is worth mentioning that a local asymptotic form of the curvature singularity can be obtained by using this complex-variable approach. Since we aim to find the local behaviour close to the singularity $\xi^* = \mathrm{i} \ln(\delta t/2)$, we write

$$\xi = \tilde{\xi} + \mathrm{i} \ln \frac{\delta t}{2}, \quad \text{for} \quad |\tilde{\xi}| \ll 1. \tag{3.32}$$

https://doi.org/10.1017/jfm.2026.11860 Published online by Cambridge University Press

Accordingly,

$$\tilde{\xi} + \mathrm{i}\ln\frac{\delta t}{2} = x - \frac{\mathrm{i}}{2}\left(1 + \frac{2\mathrm{e}^{i\tilde{\xi}}}{t}\right)t. \tag{3.33}$$

Taylor expanding the right-hand side gives

$$\tilde{\xi} + \mathrm{i}\ln\frac{\delta t}{2} = x - \frac{\mathrm{i}t}{2} - \mathrm{i}\left(1 + \mathrm{i}\tilde{\xi} - \frac{\tilde{\xi}^2}{2}\right) + O(\tilde{\xi}^3). \tag{3.34}$$

Since we are interested in solutions close to t_s, we write $t = t_s - \tau$ and assume $0 < \tau \ll 1$. Then $\tilde{\xi}$ can be expressed as

$$\tilde{\xi} \sim \sqrt{2\mathrm{i}x - \tau(1 + 2/t_s)}, \tag{3.35}$$

where we have used the identity (3.31). Eventually, we have

$$W = \delta\mathrm{e}^{i\xi} = \frac{2}{t_s - \tau}\mathrm{e}^{i\tilde{\xi}} \sim \frac{2}{t_s - \tau}\mathrm{e}^{i\sqrt{2\mathrm{i}x - \tau(1+2/t_s)}}, \quad \text{for} \quad |x| \ll 1. \tag{3.36}$$

We are interested in solutions on the real axis ($\mathrm{Im}\{x\} = 0$) at the singularity time ($\tau = 0$)

$$W \sim \frac{2}{t_s}\mathrm{e}^{i\sqrt{2ix}} = \frac{2}{t_s}\mathrm{e}^{(-1+\mathrm{sgn}(x)i)\sqrt{|x|}} \sim \frac{2}{t_s}\big(1 - (1 - \mathrm{sgn}(x)\mathrm{i})\sqrt{|x|}\big), \tag{3.37}$$

$$W_x \sim \frac{1}{t_s\sqrt{|x|}}\big(-\mathrm{sgn}(x) + \mathrm{i}\big), \tag{3.38}$$

Taking the real part leads to a local form of η_{xx}

$$\eta_{xx} \sim \frac{-\mathrm{sgn}(x)}{t_s\sqrt{|x|}}, \quad \text{for} \quad |x| \ll 1. \tag{3.39}$$

This is almost the same result as that derived by Cowley *et al.* (1999), except our t_s is replaced by their t_δ, which is solved from

$$\frac{t_\delta}{2} + \ln t_\delta = \ln\frac{1}{\delta}. \tag{3.40}$$

Note that $t_\delta \sim t_s + o(t_s)$ for $\delta \ll 1$. More detailed investigations on the properties of (3.27) is left for future studies, but we note here the simplicity of obtaining Moore's result using the Hamiltonian formulation and a DNO expansion.

To investigate the effect of the electric field on the singularity time t_s as $\delta \to 0$, we applied Moore's analysis to (3.24) and derived the following implicit expression for t_s (see Appendix C for details):

$$1 + \lambda t_s + \ln t_s + \ln\delta + \frac{1}{2}\ln\left(\frac{1}{4} + \left(\frac{E_b(1-\varepsilon)^3}{4\lambda(1+\varepsilon)^2}\right)^2\right) = 0. \tag{3.41}$$

If, however, we prescribe a different initial condition to (3.13), i.e.

$$\eta(x, 0) = \delta\sin(x), \quad \varphi(x, 0) = 0, \tag{3.42}$$

then t_s should be governed by the same equation with δ replaced by $\delta/2$

$$1 + \lambda t_s + \ln t_s + \ln\frac{\delta}{2} + \frac{1}{2}\ln\left(\frac{1}{4} + \left(\frac{E_b(1-\varepsilon)^3}{4\lambda(1+\varepsilon)^2}\right)^2\right) = 0, \tag{3.43}$$

https://doi.org/10.1017/jfm.2026.11860 Published online by Cambridge University Press

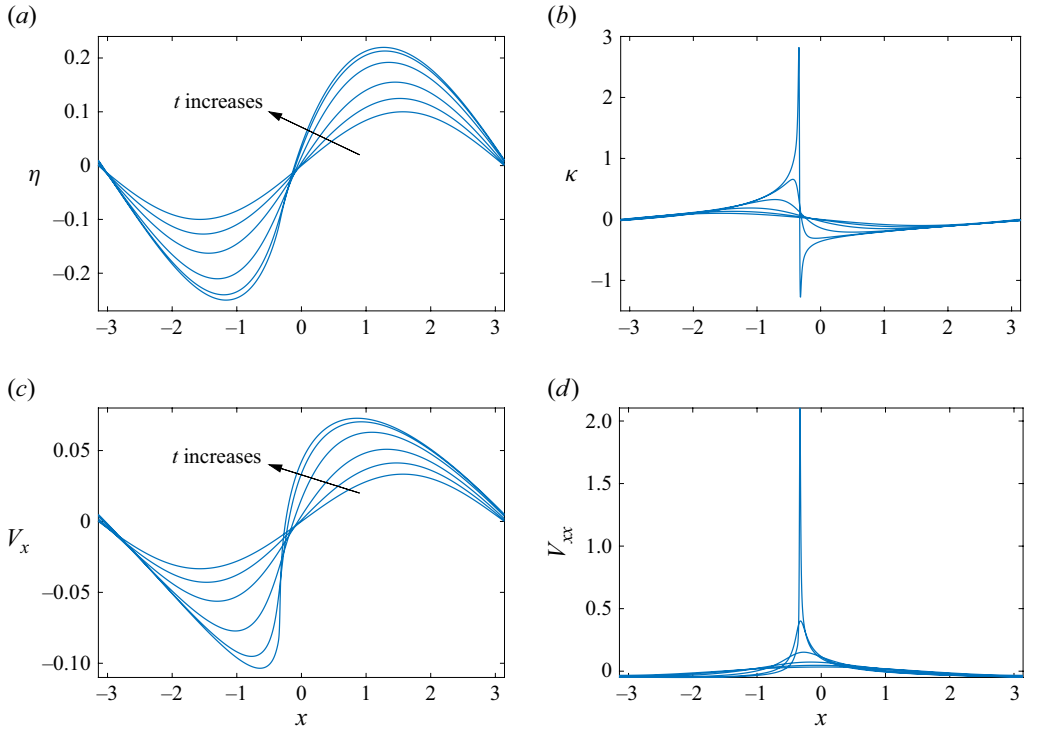


Figure 2. Results of model (3.24) for $U = 1$, $\varepsilon = 2$, $E_b = 1$ and $\delta = 0.1$ with initial condition (3.25). Panels (a–d) plot η, κ, V_x and V_{xx} at $t = 0$, 0.8, 1.6, 2.4, 2.8, 2.92.

since the initial condition now contains both growing and decaying eigenmodes with initial amplitudes of $\delta/2$, and t_s is dominated by the growing eigenmode only. In particular, (3.43) recovers Moore's result when $E_b = 0$

$$1 + \frac{t_s}{2} + \ln t_s = \ln \frac{4}{\delta}. \tag{3.44}$$

To examine the validity of (3.41), we solved the model (3.24) numerically by using a pseudospectral method in space and a fourth-order Runge–Kutta scheme in time. In figure 2, we plot solutions for $U = 1$, $\varepsilon = 2$, $E_b = 1$ (a subcritical value) and $\delta = 0.1$, with initial condition (3.25). Panels (a–d) show the interface displacement η, the curvature κ, the electric potential derivative V_x and the second derivative V_{xx}, at times $t = 0$, 0.8, 1.6, 2.4, 2.8 and 2.92. For this subcritical TEF, the results show that a curvature singularity appears at $x \approx -0.33$. The electric field destroys the odd symmetry that solutions would have in its absence given odd-parity initial conditions. Meanwhile, V_x nearly develops a shock at the same position as the curvature singularity, leading V_{xx} to blow up. To numerically estimate t_s, we used the relation

$$\|\kappa^{-1}\|_\infty = a(t_s - t) + b(t_s - t)^2, \quad \text{when} \quad t \to t_s, \tag{3.45}$$

where $\|\cdot\|_\infty$ is the L^∞ norm evaluated for $x \in [-\pi, \pi]$, and t_s, a and b are numerically fitted from the computational data by using the least-squares method. A second approach by form fitting the numerical spectrum of θ to its asymptotic form was applied

https://doi.org/10.1017/jfm.2026.11860 Published online by Cambridge University Press

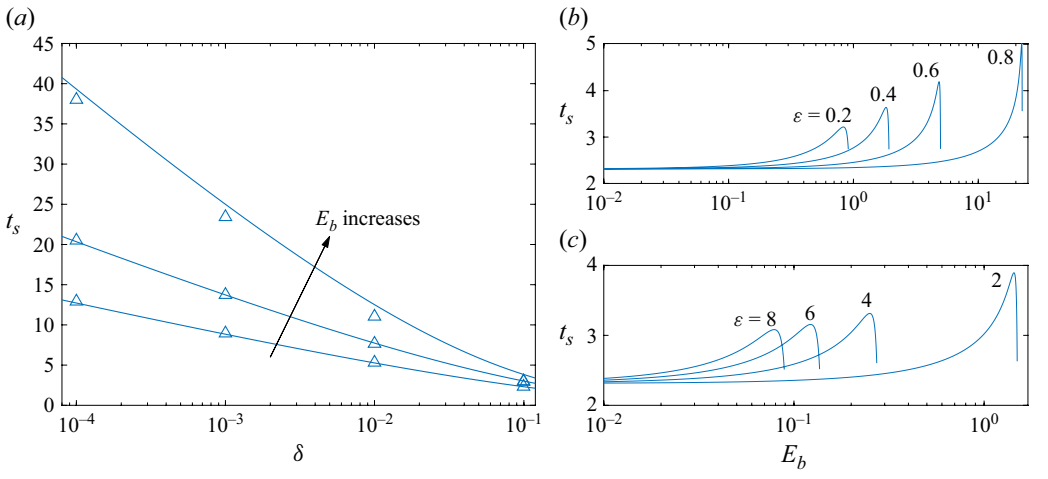


Figure 3. (*a*) Value of t_s versus δ. Triangles and solid curves are numerical results of (3.24) and (3.41) for $U = 1$ and $\varepsilon = 2$. The three groups of results correspond to $E_b = 0$, 1, 1.4 from the bottom to top. (*b–c*) Value of t_s versus E_b obtained from the (3.41) for $\delta = 0.1$.

(Krasny 1986*b*; Baker *et al.* 1993; Cowley *et al.* 1999). Here, we use the following relation:

$$|\hat{\theta}(k, t)| = \frac{A}{k^{\nu_1}} \mathrm{e}^{-\nu_2 k}, \tag{3.46}$$

and solve A, ν_1 and ν_2 by the least-squares method. Once we obtain ν_2 at different times, we can extrapolate these numerical data to estimate the moment t_s when ν_2 vanishes. It turns out that the two approaches give nearly the same estimates for t_s for most numerical solutions. We made direct comparisons of our solutions with those of Cowley *et al.* (1999), running our codes with their initial conditions. Our estimates for t_s are in complete agreement with deviations of 2 % or smaller. The largest errors appear for the smallest value of $\delta = 0.005$ used, as also pointed out by Cowley *et al.* (1999).

The dependence of t_s on δ and the electric field strength E_b is presented in figure 3. Figure 3(*a*) shows the variation of t_s with δ for $U = 1$ and $\varepsilon = 2$ for the three subcritical electric field strengths $E_b = 0$, 1, 1.4; the triangles represent t_s obtained from the numerical solution of (3.24) with initial condition (3.25), and the solid curves are the asymptotic estimates (3.41). The agreement between the numerical results and the analytical predictions is remarkable, clearly showing that $t_s \propto \ln(1/\delta)$ as $\delta \to 0$, in line with Moore's classical result. On the other hand, when E_b increases towards E_b^c, which is 1.5 for current parameters, the numerical results follow the analytic prediction qualitatively but there is a visible discrepancy. In fact, when $E_b \to E_b^c$, (3.41) yields that $t_s \to 0$ for fixed δ. This can be clearly seen from figures 3(*b*) and 3(*c*) which plot t_s versus E_b obtained from (3.41) for $\delta = 0.1$. It can be seen that t_s monotonically increases with E_b until a sudden dip appears as $E_b \to E_b^c$. This indicates that the model (3.24) breaks down because the nonlinear terms overwhelm the linear terms when $\lambda \to 0$, thus violating the basic assumption of weak nonlinearity. Full computations of the Euler equations in this regime are presented later.

3.2. *Supercritical tangential electric field, $E_b > E_b^c$*

We first recast the system (3.13) into a single equation for η

https://doi.org/10.1017/jfm.2026.11860 Published online by Cambridge University Press

$$\eta_{tt} - c^2\eta_{xx} - \frac{U}{2}\Big(2\mathrm{H}[\eta]\eta_{xt} + \mathrm{H}\big[\mathrm{H}[\eta]^2\big]_{xt}\Big)_x + \frac{E_b(1-\varepsilon)^3}{4(1+\varepsilon)^2}\Big(2\mathrm{H}[\eta]\eta_{xx} + \mathrm{H}\big[\mathrm{H}[\eta]^2\big]_{xx}\Big)_x = 0, \tag{3.47}$$

where

$$c^2 = \frac{E_b(1-\varepsilon)^2}{2(1+\varepsilon)} - \frac{1}{4} > 0. \tag{3.48}$$

In general, solutions of (3.47) contain both right- and left-travelling modes. By assuming that only one uni-directional mode dominates, the same strategy used to derive the Korteweg–de Vries equation from the Boussinesq equation, we can simplify (3.47) further. We introduce $\tau = \delta t$ and $\xi = x - ct$, and expand η asymptotically as

$$\eta \sim \eta_0(\xi, \tau) + \delta\eta_1(\xi, \tau) + \cdots. \tag{3.49}$$

The leading order of (3.47) reads

$$-2\delta c\eta_{0,\tau\xi} + 2\delta c\gamma\left(2\mathrm{H}[\eta_0]\eta_{0,\xi\xi} + \mathrm{H}\big(\mathrm{H}[\eta_0]^2\big)_{\xi\xi}\right)_\xi = O(\delta^3), \tag{3.50}$$

where

$$\gamma = \frac{E_b(1-\varepsilon)^3}{8c(1+\varepsilon)^2} + \frac{U}{4}. \tag{3.51}$$

Keeping leading-order terms and integrating (3.50) once with respect to ξ, we have a simplified equation for η_0, namely,

$$\eta_{0,\tau} - \gamma\Big(2\mathrm{H}[\eta_0]\eta_{0,\xi\xi} + \mathrm{H}\big[\mathrm{H}[\eta_0]^2\big]_{\xi\xi}\Big) = 0. \tag{3.52}$$

In arriving at (3.52) we have used the property $\mathrm{H}[fg] = \mathrm{H}[f]g + f\mathrm{H}[g] + \mathrm{H}[\mathrm{H}[f]\mathrm{H}[g]]$. The constant of integration is zero because we require conservation of mass

$$\int_0^{2\pi} \eta(\xi, \tau)\,\mathrm{d}\xi = 0. \tag{3.53}$$

We numerically solve (3.52) by using a pseudospectral method in space and a fourth-order Runge–Kutta scheme in time, as before. In the results of figure 4 we set $\gamma = 1$ and prescribe the initial condition $\eta_0(\xi, 0) = 0.1\sin(\xi)$. A parity analysis of (3.52) shows that η remains an odd function of ξ. Successive solutions from $t = 0$ to $t = 2.276$ are plotted in figure 4(*a*), showing that the interface gradually steepens on the left side of the crest. The curvature at $t = 2.276$ is plotted in figure 4(*b*), indicating the appearance of a curvature singularity. Close to the singularity time, we can seek a self-similar solution

$$\eta_0(x, t) \sim (t_s - t)^a g(\zeta), \quad \zeta = \frac{\xi}{(t_s - t)^b} = O(1), \tag{3.54}$$

where a and b are positive constants. Substituting (3.54) into (3.52), we have the balance

$$a - 2b = -1, \tag{3.55}$$

and

$$\|\kappa\|_\infty \sim \|\eta_{0,xx}\|_\infty \sim (t_s - t)^{a-2b} = (t_s - t)^{-1}. \tag{3.56}$$

Considering this relation is true only when $t_s - t \ll 1$, we can still use the assumed relation (3.45) to estimate t_s. In figure 4(*c*), we plot the inverse curvature magnitude $\|\kappa\|_\infty^{-1}$ and the least-squares fitted quadratic curve. The estimated singularity time is $t_s = 2.35$.

https://doi.org/10.1017/jfm.2026.11860 Published online by Cambridge University Press

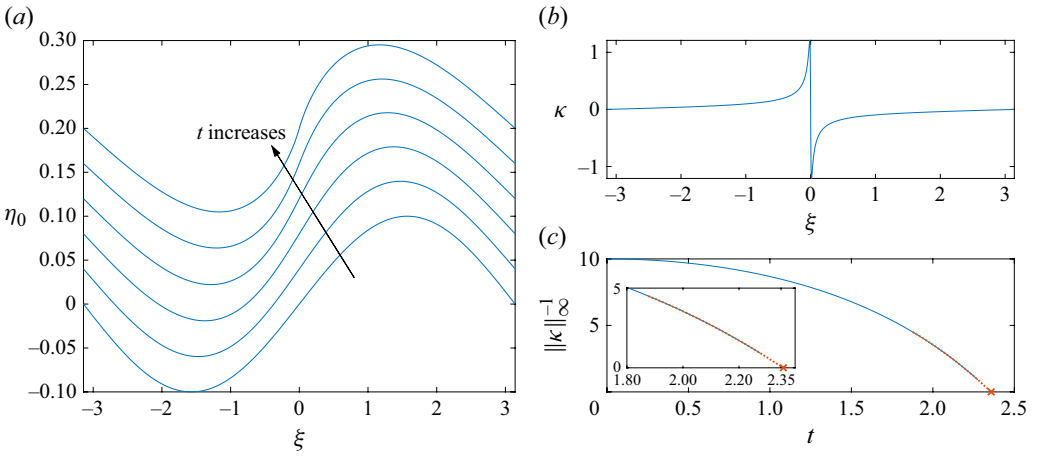


Figure 4. Numerical solution of (3.52) with $\gamma = 1$ and initial condition $\eta_0(\xi, 0) = 0.1\sin(\xi)$. (*a*) Interfaces at $t = 0$, 0.5, 1, 1.5, 2 and 2.276 from bottom to top. (*b*) Curvature profile at $t = 2.276$. (*c*) Inverse curvature amplitude versus time. The blue curve is the numerical result, and the red dotted line is the fitted curve using the quadratic relation (3.45). The red cross sign labels the estimated singularity time at $t = 2.35$.

Note that (3.52) is invariant under the transformation

$$\xi \to -\xi, \quad \gamma \to -\gamma. \tag{3.57}$$

Physically, changing the sign of ξ by reversing the direction of the ξ-axis, implies that c and U also change signs, leading to $\gamma \to -\gamma$. In particular, for initial condition $\eta(\xi, 0) = 0.1\sin(\xi)$ and $\gamma = -1$, the interface steepens on the right side of the crest. In general, the transformation

$$\eta_0 \to \delta\eta_0, \quad t \to \frac{t}{\delta|\gamma|}, \tag{3.58}$$

rescales the initial amplitude to 1, and γ to 1 if it is positive, or -1 otherwise. Therefore, the singularity time is inversely proportional to $\delta|\gamma|$. For initial condition $\eta_0(\xi, 0) = \delta\sin(\xi)$, the result in figure 4 gives an estimate of the singularity time to be

$$t_s = \frac{0.235}{\delta}\left|\frac{E_b(1-\varepsilon)^3}{8c(1+\varepsilon)^2} + \frac{U}{4}\right|^{-1}. \tag{3.59}$$

Note that (3.52) is derived under the assumption that only one uni-directional component dominates. For model (3.13), this is guaranteed by giving the following initial conditions:

$$\eta(x, 0) = \delta\sin(x), \quad \varphi(x, 0) = -2\delta c\cos(x). \tag{3.60}$$

If, however, the initial conditions are

$$\eta(x, 0) = \delta\sin(x), \quad \varphi(x, 0) = 0, \tag{3.61}$$

there coexist two counter-travelling modes. Depending on the values of U and ε, the singularity first develops in the component travelling at a speed of $\mathrm{sgn}((1-\varepsilon)U)|c|$. With $U > 0$, which is the case we focus on, a curvature singularity forms and travels to the left (right) for $\varepsilon > 1$ ($\varepsilon < 1$). Thus, an estimate of the singularity time is

$$t_s = \frac{0.47}{\delta}\left(\left|\frac{E_b(1-\varepsilon)^3}{8c(1+\varepsilon)^2}\right| + \frac{|U|}{4}\right)^{-1}. \tag{3.62}$$

https://doi.org/10.1017/jfm.2026.11860 Published online by Cambridge University Press

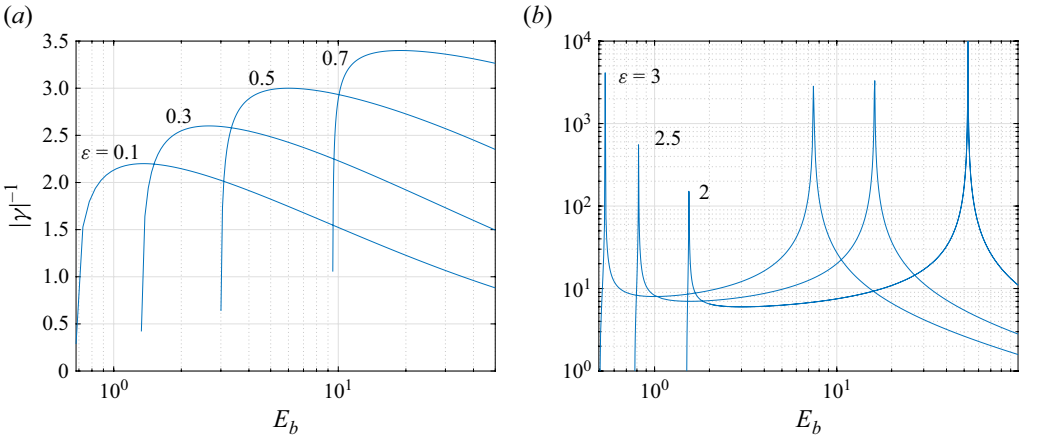


Figure 5. Typical plots of $|\gamma|^{-1}$ versus E_b for $cU > 0$: (*a*) $\varepsilon < 1$; (*b*) $\varepsilon > 1$.

Note that Moore's analysis is not adequate for model (3.52) because this method requires $t_s = o(1/\delta)$ (see Appendix C). For model (3.52), however, it is clear that $t_s \propto 1/\delta$, which makes the asymptotic expansion non-uniformly valid when $t \to t_s$.

Depending on the values of c, U, and ε, $|\gamma|^{-1}$ either remains bounded or blows up at some specfici values of E_b. In general, we have the following results that arise directly from (3.51):

$$\max\{|\gamma|^{-1}\} = \begin{cases} \infty, & \text{at } E_b = \dfrac{(1+\varepsilon)^2(1\pm\sqrt{\varepsilon})^2}{(1-\varepsilon)^4}, \quad \text{when } cU > 0,\ \varepsilon > 1, \\ \infty, & \text{at } E_b = \dfrac{(1+\varepsilon)^2(1\pm\sqrt{\varepsilon})^2}{(1-\varepsilon)^4}, \quad \text{when } cU < 0,\ \varepsilon < 1, \\ 2(1+\varepsilon), & \text{at } E_b = \dfrac{(1+\varepsilon)}{(1-\varepsilon)^2}, \quad \text{when } cU > 0,\ \varepsilon < 1, \\ \dfrac{2(1+\varepsilon)}{\varepsilon}, & \text{at } E_b = \dfrac{(1+\varepsilon)}{(1-\varepsilon)^2}, \quad \text{when } cU < 0,\ \varepsilon > 1. \end{cases} \tag{3.63}$$

It is worth mentioning that the two cases $cU > 0$ and $cU < 0$ can be transformed to each other by using the transformations

$$U \to -U, \quad \varepsilon \to \frac{1}{\varepsilon}, \quad E_b \to \varepsilon E_b, \tag{3.64}$$

which can be interpreted as turning the two-layer system upside down. Since the definition of E_b relies on the permittivity constant of the lower fluid, a factor ε emerges when we flip the system. Equation (3.63) indicates that the curvature singularity may be significantly delayed when E_b is close to the values that lead $|\gamma|^{-1}$ to blow up. Strictly speaking, however, when $|\gamma| = O(\delta)$, the cubic nonlinearity becomes equally important as the quadratic one, meaning that (3.52) is no longer an asymptotically valid model. Although the precise behaviour of solutions in this regime is unclear, i.e. whether the curvature singularity can be suppressed by a possible saturation arising from the cubic nonlinearity, it is certain that t_s becomes significantly large, typically $O(1/\delta^2)$, and we shall confirm this assertion later in solutions of the Euler equations. Figure 5 plots some typical $|\gamma|^{-1}$ curves for $cU > 0$. It is interesting to note that these curves indicate that t_s decreases with

https://doi.org/10.1017/jfm.2026.11860 Published online by Cambridge University Press

E_b when it becomes sufficiently large. When $E_b \to \infty$

$$t_s \propto \frac{1}{\sqrt{E_b}}. \tag{3.65}$$

At this stage the legitimacy of this estimate is unclear, as is also the prediction that $t_s \to 0$ when $E_b \to E_b^c$. For similar reasons to those mentioned in § 5.2, i.e. when $|\gamma| = O(1/\delta)$, the leading quadratic nonlinearity becomes as important as the linear terms, which may violate the basic weakly nonlinear assumption used to derive the model (3.13). Nevertheless, we shall check the validity of these asymptotic estimates in comparisons with full Euler simulations.

4. Boundary integral methods for Euler-electrostatics systems

In this section, we present a time-dependent algorithm to simulate the fully nonlinear evolution of electrified vortex sheets. The formulation is based on the $\theta - s_\alpha$ Lagrangian framework coupled with the BIM using the Cauchy integral formula.

4.1. *The $\theta - s_\alpha$ Lagrangian formulation*

We parameterise the interface by a Lagrangian parameter $\alpha \in [0, 1]$. It is well known that for a two-dimensional material curve, its tangent angle $\theta(\alpha, t)$ and arclength derivative $s_\alpha(\alpha, t)$ are governed by the following $\theta - s_\alpha$ formulation (see Yang 1992; Hou *et al.* 1994, 1997; Guan & Vanden-Broeck 2025):

$$\theta_t = \frac{N_\alpha}{s_\alpha} + \frac{\theta_\alpha T}{s_\alpha}, \tag{4.1}$$

$$s_{\alpha t} = T_\alpha - \theta_\alpha N, \tag{4.2}$$

where T and N represent the tangential and normal velocities that are defined below. Using the relation

$$\frac{z_\alpha}{s_\alpha} = \mathrm{e}^{i\theta}, \quad z(\alpha, t) = x(\alpha, t) + \mathrm{i}\eta(\alpha, t), \tag{4.3}$$

one can construct the interface by the following integration:

$$z(\alpha, t) = \int_0^\alpha \mathrm{e}^{i\theta(\alpha', t)} s_\alpha(\alpha', t)\, \mathrm{d}\alpha' + z_0. \tag{4.4}$$

The function $z_0 = z(0, t) = x_0 + \mathrm{i}\eta_0$ is the complex coordinate of the leftmost Lagrangian marker, hence

$$z_{0,t} = \big(T(0, t) + \mathrm{i}N(0, t)\big)\mathrm{e}^{i\theta(0,t)}. \tag{4.5}$$

The tangential and normal velocities of the lower and upper fluid particles on the interface are

$$T_j = -(-1)^j \frac{U}{2}\cos\theta + \frac{\partial \phi_j}{\partial \boldsymbol{t}}, \quad N = (-1)^j \frac{U}{2}\sin\theta + \frac{\partial \phi_j}{\partial \boldsymbol{n}}, \quad \text{for } j = 1 \text{ and } 2. \tag{4.6}$$

Note that the normal velocity is continuous across the interface, so we can drop the subscript. On the other hand, $T_1 \neq T_2$, so there is freedom to define T in (4.1) and (4.2). Following Baker *et al.* (1982) and Grue *et al.* (1997), we write T as a linear combination of T_1 and T_2

$$T = \beta T_1 + (1 - \beta)T_2, \tag{4.7}$$

https://doi.org/10.1017/jfm.2026.11860 Published online by Cambridge University Press

where $\beta \in [0, 1]$. Note that $\beta = 0$ or 1 corresponds to choosing the upper or the lower fluid particles as the Lagrangian markers, respectively. In our simulations, we find that $\beta = 0.5$ is the best choice for subcritical electric fields (this is also the usual choice in the Birkhoff–Rott equation). For supercritical electric fields, however, there is no general way to choose the optimal value of β. Here by optimal, we mean the specific value of β such that s_α takes a global minimum value at the singular point among all choices. In this case, we test different values of β and take the one giving the smallest energy error (4.52).

Defining $\varphi_j(\alpha, t) = \phi_j(x(\alpha, t), \eta(\alpha, t), t)$, we have

$$\varphi_{j,t} = \frac{D\phi_j}{Dt} = \phi_{j,t} + T\frac{\partial \phi_j}{\partial \boldsymbol{t}} + N\frac{\partial \phi_j}{\partial \boldsymbol{n}}, \quad \text{for} \quad j = 1 \text{ and } 2, \tag{4.8}$$

where D/Dt denotes the material derivative associated with the Lagrangian markers. The dimensionless Bernoulli equation is expressed as

$$\varphi_t - T\left[\frac{\partial \phi_1}{\partial \boldsymbol{t}} - R\frac{\partial \phi_2}{\partial \boldsymbol{t}}\right] - N\left[\frac{\partial \phi_1}{\partial \boldsymbol{n}} - R\frac{\partial \phi_2}{\partial \boldsymbol{n}}\right] + \frac{T_1^2 + N^2}{2} - R\frac{T_2^2 + N^2}{2} + \frac{1 - R}{F_r^2}\eta + \frac{E_b}{2}\big[\boldsymbol{n} \cdot \boldsymbol{\Sigma} \cdot \boldsymbol{n}\big]_2^1 = 0, \tag{4.9}$$

where $\varphi(\alpha, t) = \varphi_1(\alpha, t) - R\varphi_2(\alpha, t)$. Using relations (4.6), we have

$$\varphi_t + \frac{1 - 2\beta}{2}\big(T_1^2 + RT_2^2\big) - \big(1 - \beta - R\beta\big)T_1T_2 - \frac{1 - R}{2}N^2 + \frac{U}{2}(1 + R)\big(T\cos\theta - N\sin\theta\big) + \frac{1 - R}{F_r^2}\eta + \frac{E_b}{2}\big[\boldsymbol{n} \cdot \boldsymbol{\Sigma} \cdot \boldsymbol{n}\big]_2^1 = 0, \tag{4.10}$$

where

$$\big[\boldsymbol{n} \cdot \boldsymbol{\Sigma} \cdot \boldsymbol{n}\big]_2^1 = \left(\frac{\partial V_1}{\partial \boldsymbol{n}} - \sin\theta\right)^2 - \left(\frac{\partial V_1}{\partial \boldsymbol{t}} + \cos\theta\right)^2 - \varepsilon\left(\frac{\partial V_1}{\partial \boldsymbol{n}} - \sin\theta\right)^2 + \varepsilon\left(\frac{\partial V_1}{\partial \boldsymbol{t}} + \cos\theta\right)^2. \tag{4.11}$$

Therefore, we have four time-evolution equations (4.1), (4.2), (4.5) and (4.10) for the unknowns θ, s_α, z_0 and φ.

4.2. *The Cauchy integral formula and derivation of integral equations of the second kind*

In each fluid layer we define the complex velocity

$$w_j = \phi_{j,x} - \mathrm{i}\phi_{j,y}, \quad \text{for } j = 1 \text{ and } 2. \tag{4.12}$$

They are analytic functions and satisfy Cauchy's integral formula

$$w_j(z_0) = \frac{1}{\pi \mathrm{i}}\mathrm{PV}\oint_{C_j}\frac{w_j(z)}{z - z_0}\,\mathrm{d}z, \quad \text{for } j = 1 \text{ and } 2, \tag{4.13}$$

where PV denotes the Cauchy principal value, z and z_0 are points on the interface and C_1 and C_2 are contours along the interface such that the fluid 1 and 2 are on their left side. Alternatively, we use the transformation $\zeta = \mathrm{e}^{-\mathrm{i}z}$ to cast (4.13) into

$$w_j(\zeta_0) = \frac{1}{\pi \mathrm{i}}\mathrm{PV}\oint_{\Omega_j}\frac{w_j(\zeta)}{\zeta - \zeta_0}\,\mathrm{d}\zeta, \quad \text{for } j = 1 \text{ and } 2. \tag{4.14}$$

https://doi.org/10.1017/jfm.2026.11860 Published online by Cambridge University Press

The new contours Ω_1 and Ω_2 are the images of C_1 and C_2, and become closed under the transformation. Using (4.3) and the identities

$$w_j \, \mathrm{e}^{i\theta} = \frac{\partial \phi_j}{\partial \boldsymbol{t}} - \mathrm{i}\frac{\partial \phi_j}{\partial \boldsymbol{n}}, \quad \text{for } j = 1 \text{ and } 2, \tag{4.15}$$

we can rewrite (4.14) as

$$\frac{\partial \phi_1}{\partial \boldsymbol{t}}(\alpha') - \mathrm{i}\frac{\partial \phi_1}{\partial \boldsymbol{n}}(\alpha') = \frac{1}{\pi}\int_0^1 \frac{\mathrm{e}^{i\theta(\alpha')} s_\alpha(\alpha)}{1 - \mathrm{e}^{i(z(\alpha)-z(\alpha'))}} \left(\frac{\partial \phi_1}{\partial \boldsymbol{t}}(\alpha) - \mathrm{i}\frac{\partial \phi_1}{\partial \boldsymbol{n}}(\alpha) \right) \mathrm{d}\alpha, \tag{4.16}$$

$$\frac{\partial \phi_2}{\partial \boldsymbol{t}}(\alpha') - \mathrm{i}\frac{\partial \phi_2}{\partial \boldsymbol{n}}(\alpha') = -\frac{1}{\pi}\int_0^1 \frac{\mathrm{e}^{i\theta(\alpha')} s_\alpha(\alpha)}{1 - \mathrm{e}^{i(z(\alpha)-z(\alpha'))}} \left(\frac{\partial \phi_2}{\partial \boldsymbol{t}}(\alpha) - \mathrm{i}\frac{\partial \phi_2}{\partial \boldsymbol{n}}(\alpha) \right) \mathrm{d}\alpha, \tag{4.17}$$

where we have dropped the PV for brevity. Similarly, the voltage potentials satisfy the following analogous equations:

$$\frac{\partial V_1}{\partial \boldsymbol{t}}(\alpha') - \mathrm{i}\frac{\partial V_1}{\partial \boldsymbol{n}}(\alpha') = \frac{1}{\pi}\int_0^1 \frac{\mathrm{e}^{i\theta(\alpha')} s_\alpha(\alpha)}{1 - \mathrm{e}^{i(z(\alpha)-z(\alpha'))}} \left(\frac{\partial V_1}{\partial \boldsymbol{t}}(\alpha) - \mathrm{i}\frac{\partial V_1}{\partial \boldsymbol{n}}(\alpha) \right) \mathrm{d}\alpha, \tag{4.18}$$

$$\frac{\partial V_2}{\partial \boldsymbol{t}}(\alpha') - \mathrm{i}\frac{\partial V_2}{\partial \boldsymbol{n}}(\alpha') = -\frac{1}{\pi}\int_0^1 \frac{\mathrm{e}^{i\theta(\alpha')} s_\alpha(\alpha)}{1 - \mathrm{e}^{i(z(\alpha)-z(\alpha'))}} \left(\frac{\partial V_2}{\partial \boldsymbol{t}}(\alpha) - \mathrm{i}\frac{\partial V_2}{\partial \boldsymbol{n}}(\alpha) \right) \mathrm{d}\alpha. \tag{4.19}$$

These integral equations must be solved with appropriate boundary conditions. Since φ is given as initial condition, we have

$$\frac{\partial \phi_1}{\partial \boldsymbol{t}} - R\frac{\partial \phi_2}{\partial \boldsymbol{t}} = \frac{\varphi_\alpha}{s_\alpha}. \tag{4.20}$$

The normal velocity N is continuous across the interface, thus giving

$$\frac{\partial \phi_1}{\partial \boldsymbol{n}} - \frac{\partial \phi_2}{\partial \boldsymbol{n}} = U \sin\theta. \tag{4.21}$$

For the voltage potentials, we define $V(\alpha, t) = V_1(x(\alpha, t), \eta(\alpha, t), t) = V_2(x(\alpha, t), \eta(\alpha, t), t)$. The tangential derivatives must be identical, meaning

$$\frac{\partial V_1}{\partial \boldsymbol{t}} = \frac{\partial V_2}{\partial \boldsymbol{t}} = \frac{\partial V}{\partial \boldsymbol{t}}. \tag{4.22}$$

For their normal derivatives, (2.10) gives

$$\frac{\partial V_1}{\partial \boldsymbol{n}} - \varepsilon\frac{\partial V_2}{\partial \boldsymbol{n}} = (1 - \varepsilon)\sin\theta. \tag{4.23}$$

These are appropriate boundary conditions for (4.16)–(4.19). We illustrate how to embed them into the boundary integral equations for (4.16) and (4.17). Separating the real and imaginary parts, we have

$$\frac{\partial \phi_1}{\partial \boldsymbol{n}}(\alpha') = \int_0^1 \left(\mathcal{A}(\alpha', \alpha)\frac{\partial \phi_1}{\partial \boldsymbol{n}}(\alpha) - \mathcal{B}(\alpha', \alpha)\frac{\partial \phi_1}{\partial \boldsymbol{t}}(\alpha) \right) \mathrm{d}\alpha, \tag{4.24}$$

$$\frac{\partial \phi_2}{\partial \boldsymbol{n}}(\alpha') = \int_0^1 \left(\mathcal{B}(\alpha', \alpha)\frac{\partial \phi_2}{\partial \boldsymbol{t}}(\alpha) - \mathcal{A}(\alpha', \alpha)\frac{\partial \phi_2}{\partial \boldsymbol{n}}(\alpha) \right) \mathrm{d}\alpha, \tag{4.25}$$

$$\frac{\partial \phi_1}{\partial \boldsymbol{t}}(\alpha') = \int_0^1 \left(\mathcal{A}(\alpha', \alpha)\frac{\partial \phi_1}{\partial \boldsymbol{t}}(\alpha) + \mathcal{B}(\alpha', \alpha)\frac{\partial \phi_1}{\partial \boldsymbol{n}}(\alpha) \right) \mathrm{d}\alpha, \tag{4.26}$$

https://doi.org/10.1017/jfm.2026.11860 Published online by Cambridge University Press

$$\frac{\partial \phi_2}{\partial \boldsymbol{t}}(\alpha') = -\int_0^1 \left(\mathcal{A}(\alpha', \alpha) \frac{\partial \phi_2}{\partial \boldsymbol{t}}(\alpha) + \mathcal{B}(\alpha', \alpha) \frac{\partial \phi_2}{\partial \boldsymbol{n}}(\alpha) \right) \mathrm{d}\alpha, \tag{4.27}$$

where

$$\mathcal{A}(\alpha', \alpha) = \frac{1}{\pi} \mathrm{Re}\left(\frac{\mathrm{e}^{i\theta(\alpha')} s_\alpha(\alpha)}{1 - \mathrm{e}^{i(z(\alpha) - z(\alpha'))}} \right), \quad \mathcal{B}(\alpha', \alpha) = \frac{1}{\pi} \mathrm{Im}\left(\frac{\mathrm{e}^{i\theta(\alpha')} s_\alpha(\alpha)}{1 - \mathrm{e}^{i(z(\alpha) - z(\alpha'))}} \right). \tag{4.28}$$

We introduce

$$\mathcal{T} = \frac{\partial \phi_1}{\partial \boldsymbol{t}} - R \frac{\partial \phi_2}{\partial \boldsymbol{t}}, \quad \mathcal{U} = \frac{\partial \phi_1}{\partial \boldsymbol{t}} + \frac{\partial \phi_2}{\partial \boldsymbol{t}}, \quad \mathcal{J} = \frac{\partial \phi_1}{\partial \boldsymbol{n}} - \frac{\partial \phi_2}{\partial \boldsymbol{n}}, \quad \mathcal{Q} = \frac{\partial \phi_1}{\partial \boldsymbol{n}} + R \frac{\partial \phi_2}{\partial \boldsymbol{n}}, \tag{4.29}$$

to express the original unknowns as

$$\frac{\partial \phi_1}{\partial \boldsymbol{t}} = \frac{\mathcal{T} + R\mathcal{U}}{1 + R}, \quad \frac{\partial \phi_2}{\partial \boldsymbol{t}} = \frac{\mathcal{U} - \mathcal{T}}{1 + R}, \quad \frac{\partial \phi_1}{\partial \boldsymbol{n}} = \frac{\mathcal{Q} + R\mathcal{J}}{1 + R}, \quad \frac{\partial \phi_2}{\partial \boldsymbol{n}} = \frac{\mathcal{Q} - \mathcal{J}}{1 + R}. \tag{4.30}$$

Multiplying (4.25) by R and adding it to (4.24), we have

$$\mathcal{Q}(\alpha') = \frac{1 - R}{1 + R} \int_0^1 \mathcal{A}(\alpha', \alpha) \mathcal{Q}(\alpha)\, \mathrm{d}\alpha + \underbrace{\frac{2R}{1 + R} \int_0^1 \mathcal{A}(\alpha', \alpha) \mathcal{J}(\alpha)\, \mathrm{d}\alpha - \int_0^1 \mathcal{B}(\alpha', \alpha) \mathcal{T}(\alpha)\, \mathrm{d}\alpha}_{\mathcal{T} \text{ and } \mathcal{J} \text{ are known from (4.20) and (4.21)}}. \tag{4.31}$$

Adding (4.26) to (4.27), we obtain

$$\mathcal{U}(\alpha') = \frac{R - 1}{1 + R} \int_0^1 \mathcal{A}(\alpha', \alpha) \mathcal{U}(\alpha)\, \mathrm{d}\alpha + \underbrace{\frac{2}{1 + R} \int_0^1 \mathcal{A}(\alpha', \alpha) \mathcal{T}(\alpha)\, \mathrm{d}\alpha + \int_0^1 \mathcal{B}(\alpha', \alpha) \mathcal{J}(\alpha)\, \mathrm{d}\alpha}_{\mathcal{T} \text{ and } \mathcal{J} \text{ are known from (4.20) and (4.21)}}. \tag{4.32}$$

Similarly, after introducing

$$\mathcal{S} = \frac{\partial V_1}{\partial \boldsymbol{n}} - \varepsilon \frac{\partial V_2}{\partial \boldsymbol{n}}, \quad \mathcal{W} = \frac{\partial V_1}{\partial \boldsymbol{n}} + \frac{\partial V_2}{\partial \boldsymbol{n}}, \tag{4.33}$$

(4.18) and (4.19) can be rewritten as

$$\mathcal{W}(\alpha') = \frac{\varepsilon - 1}{1 + \varepsilon} \int_0^1 \mathcal{A}(\alpha', \alpha) \mathcal{W}(\alpha)\, \mathrm{d}\alpha + \underbrace{\frac{2}{1 + \varepsilon} \int_0^1 \mathcal{A}(\alpha', \alpha) \mathcal{S}(\alpha)\, \mathrm{d}\alpha}_{\mathcal{S} \text{ is known from (4.23)}}, \tag{4.34}$$

$$\frac{\partial V}{\partial \boldsymbol{t}}(\alpha') = \frac{1 - \varepsilon}{1 + \varepsilon} \int_0^1 \mathcal{A}(\alpha', \alpha) \frac{\partial V}{\partial \boldsymbol{t}}(\alpha)\, \mathrm{d}\alpha + \underbrace{\frac{1}{1 + \varepsilon} \int_0^1 \mathcal{B}(\alpha', \alpha) \mathcal{S}(\alpha)\, \mathrm{d}\alpha}_{\mathcal{S} \text{ is known from (4.23)}}. \tag{4.35}$$

The normal derivatives of the voltage potentials can be calculated from

$$\frac{\partial V_1}{\partial \boldsymbol{n}} = \frac{\mathcal{S} + \varepsilon \mathcal{W}}{1 + \varepsilon}, \quad \frac{\partial V_2}{\partial \boldsymbol{n}} = \frac{\mathcal{W} - \mathcal{S}}{1 + \varepsilon}. \tag{4.36}$$

Therefore, we obtain four decoupled Fredholm integral equations of the second kind. In particular, (4.31) and (4.25) are automatically solved when $R = 1$. It is worth mentioning that the current boundary integral formulation can be readily applied to flows with flat or uneven solid boundaries. Interested readers are referred to Guan & Vanden-Broeck (2025) for more details.

https://doi.org/10.1017/jfm.2026.11860 Published online by Cambridge University Press

4.3. *Numerical implementation*

We introduce M Lagrangian markers

$$\alpha_m = \frac{m}{M}, \quad m = 0, 1, \cdots, M-1. \tag{4.37}$$

All spatial derivatives and integrations are calculated using fast Fourier transforms (FFTs). When constructing the interface from (4.4), x and η are calculated via

$$x(\alpha, t) = \int_0^\alpha \cos\big(\theta(\alpha', t)\big) s_\alpha(\alpha', t)\, \mathrm{d}\alpha' + x_0, \tag{4.38}$$

$$\eta(\alpha, t) = \int_0^\alpha \sin\big(\theta(\alpha', t)\big) s_\alpha(\alpha', t)\, \mathrm{d}\alpha' + \eta_0. \tag{4.39}$$

Note that directly evaluating (4.38) may violate the periodicity condition

$$x(1, t) - x(0, t) = 2\pi, \tag{4.40}$$

because this requires the mean of $\cos(\theta(\alpha, t)) s_\alpha(\alpha, t)$ to be exactly 2π. Following Ambrose *et al.* (2022), we rewrite (4.38) as

$$x(\alpha, t) = \int_0^\alpha \mathcal{P}\big(\cos\big(\theta(\alpha', t)\big) s_\alpha(\alpha', t)\big)\, \mathrm{d}\alpha' + 2\pi\alpha + x_0, \tag{4.41}$$

where $\mathcal{P}$ is the zero-mean operator

$$\mathcal{P}\big(f(\alpha)\big) = f(\alpha) - \int_0^1 f(\alpha)\, \mathrm{d}\alpha. \tag{4.42}$$

Once the interface is computed, the boundary integral (4.31)–(4.35) can be solved. Note that when $\alpha \to \alpha_m$

$$\frac{\mathrm{e}^{i\theta(\alpha_m)} s_\alpha(\alpha)}{1 - \mathrm{e}^{i(z(\alpha) - z(\alpha_m))}} = \frac{\mathrm{i}}{\alpha - \alpha_m} + \frac{\mathrm{i} s_{\alpha\alpha}(\alpha_m)}{2 s_\alpha(\alpha_m)} + \frac{s_\alpha(\alpha_m)\mathrm{e}^{i\theta(\alpha_m)}}{2} + \frac{\theta_\alpha(\alpha_m)}{2} + O(\alpha - \alpha_m). \tag{4.43}$$

Therefore, $\mathcal{B}(\alpha_m, \alpha)$ is singular at $\alpha = \alpha_m$. For a smooth periodic function $f(\alpha)$

$$\int_0^1 \mathcal{B}(\alpha_m, \alpha) f(\alpha)\, \mathrm{d}\alpha = \int_{\alpha_m - \frac{1}{2}}^{\alpha_m + \frac{1}{2}} \left[\mathcal{B}(\alpha_m, \alpha) f(\alpha) - \frac{f(\alpha_m)}{\pi(\alpha - \alpha_m)}\right] \mathrm{d}\alpha + \underbrace{\frac{f(\alpha_m)}{\pi} \mathrm{PV} \int_{\alpha_m - \frac{1}{2}}^{\alpha_m + \frac{1}{2}} \frac{1}{\alpha - \alpha_m}\, \mathrm{d}\alpha}_{0}, \tag{4.44}$$

where the integrals are understood to be principal valued, and we have used periodicity to change the lower and upper limits. The first integrand on the right-hand side of (4.44) becomes regular and tends to f_α/π when $\alpha \to \alpha_m$. The trapezoid rule below provides spectral accuracy

$$\int_0^1 \mathcal{B}(\alpha_m, \alpha) f(\alpha)\, \mathrm{d}\alpha \approx \frac{1}{M} \sum_{n=0, n\neq m}^{M-1} \mathcal{B}(\alpha_m, \alpha_n) f(\alpha_n) + \frac{f_\alpha(\alpha_m)}{\pi M}. \tag{4.45}$$

https://doi.org/10.1017/jfm.2026.11860 Published online by Cambridge University Press

Therefore, the discretised boundary integral (4.31)–(4.35) can be written in compact form as follows:

$$\begin{bmatrix} \mathbb{I}-\dfrac{1-R}{1+R}\mathbb{A} & 0 & 0 & 0 \\ 0 & \mathbb{I}+\dfrac{1-R}{1+R}\mathbb{A} & 0 & 0 \\ 0 & 0 & \mathbb{I}+\dfrac{1-\varepsilon}{1+\varepsilon}\mathbb{A} & 0 \\ 0 & 0 & 0 & \mathbb{I}-\dfrac{1-\varepsilon}{1+\varepsilon}\mathbb{A} \end{bmatrix} \begin{bmatrix} \mathcal{Q}^m \\ \mathcal{U}^m \\ \mathcal{W}^m \\ \left(\dfrac{\partial V}{\partial \boldsymbol{t}}\right)^m \end{bmatrix}$$

$$= \begin{bmatrix} \dfrac{2R}{1+R}\mathbb{A}\mathcal{J}^m - \mathbb{B}\mathcal{T}^m \\ \dfrac{2}{1+R}\mathbb{A}\mathcal{T}^m + \mathbb{B}\mathcal{J}^m \\ \dfrac{2}{1+\varepsilon}\mathbb{A}\mathcal{S}^m \\ \dfrac{1}{1+\varepsilon}\mathbb{B}\mathcal{S}^m \end{bmatrix} + \begin{bmatrix} -\dfrac{1}{\pi M}(T_\alpha)^m \\ \dfrac{1}{\pi M}(J_\alpha)^m \\ 0 \\ \dfrac{1}{\pi M(1+\varepsilon)}(S_\alpha)^m \end{bmatrix}, \tag{4.46}$$

where the superscript m denotes evaluation at $\alpha=\alpha_m$, $(m=1,2,\cdots,M-1)$, $\mathbb{I}$ is the $M\times M$ identity matrix and $\mathbb{A}$ and $\mathbb{B}$ are defined as

$$\mathbb{A}_{mn} = \begin{cases} \dfrac{\mathcal{A}(\alpha_m,\alpha_n)}{M}, & m\neq n, \\ \dfrac{s_\alpha(\alpha_m)\cos\big(\theta(\alpha_m)\big)+\theta_\alpha(\alpha_m)}{2M}, & m=n, \end{cases} \tag{4.47}$$

$$\mathbb{B}_{mn} = \begin{cases} \dfrac{\mathcal{B}(\alpha_m,\alpha_n)}{M}, & m\neq n, \\ \dfrac{s_{\alpha\alpha}(\alpha_m)}{2Ms_\alpha(\alpha_m)}+\dfrac{s_\alpha(\alpha_m)\sin\big(\theta(\alpha_m)\big)}{2M}, & m=n. \end{cases} \tag{4.48}$$

Note that the first two diagonal blocks degenerate to the identity matrix when $R=1$, reflecting the fact that $\mathcal{Q}^m$ and $\mathcal{U}^m$ are already solved in this case. For $\mathcal{W}^m$ and $(\partial V/\partial \boldsymbol{t})^m$, we use the GMRES solver with a residual tolerance 10^{-11}.

Time integration of (4.1), (4.2), (4.5) and (4.10) is performed with a fourth-order Runge–Kutta method. Higher-order time-marching algorithms have been tested but we found that the fourth-order method balances accuracy and efficiency quite well.

To control aliasing errors we implemented and used both a Krasny filter $\mathcal{K}_1$ (Krasny 1986*b*)

$$\mathcal{K}_1\big(\hat{f}(k)\big) = \begin{cases} \hat{f}(k), & |\hat{f}(k)|>10^{-11}, \\ 0, & |\hat{f}(k)|\leqslant 10^{-11}, \end{cases} \tag{4.49}$$

and a 36th-order exponentially decaying filter $\mathcal{K}_2$ (Hou & Li 2007)

$$\mathcal{K}_2\big(\hat{f}(k)\big) = \hat{f}(k)\exp\big(-36(k/k_{max})^{36}\big), \tag{4.50}$$

https://doi.org/10.1017/jfm.2026.11860 Published online by Cambridge University Press

where $\hat{f}(k)$ denotes the Fourier transform of $f(\alpha)$, and k_{max} is the Nyquist wavenumber. Here, $\mathcal{K}_1$ is applied at every time after performing the FFT, and $\mathcal{K}_2$ is used at the end of each Runge–Kutta step.

Calculations were typically started with $M = 64$ and $\Delta t = 0.005$. When the amplitude of the last 20 % of $\hat{\theta}(k)$ exceeds 10^{-8}, the solution is spectrally interpolated by doubling or quadrupling M. Simultaneously, Δt is halved or quartered to prevent aliasing. This process continues until M reaches a predefined value, typically 8192.

The Hamiltonian $\mathcal{H}$ given in § 3 is a conserved quantity, and it was used to monitor our numerical accuracy. An equivalent form of $\mathcal{H}$ is

$$\begin{aligned}\mathcal{H}(t) = &\frac{1}{2}\int_0^1 \varphi_1 \frac{\partial \phi_1}{\partial \boldsymbol{n}} s_\alpha \,\mathrm{d}\alpha - \frac{U}{2}\int_0^1 \varphi_1 s_\alpha \sin\theta \,\mathrm{d}\alpha - \frac{R}{2}\int_0^1 \varphi_2 \frac{\partial \phi_2}{\partial \boldsymbol{n}} s_\alpha \,\mathrm{d}\alpha \\ &- \frac{RU}{2}\int_0^1 \varphi_2 s_\alpha \sin\theta \,\mathrm{d}\alpha + \frac{1-R}{2F_r^2}\int_0^1 \eta^2 s_\alpha \cos\theta \,\mathrm{d}\alpha \\ &+ \frac{E_b}{2}\int_0^1 V \frac{\partial V_1}{\partial \boldsymbol{n}} s_\alpha \,\mathrm{d}\alpha - \frac{E_b\varepsilon}{2}\int_0^1 V \frac{\partial V_2}{\partial \boldsymbol{n}} s_\alpha \,\mathrm{d}\alpha. \end{aligned} \tag{4.51}$$

We define its relative error

$$\mathcal{H}_r(t) = \left|\frac{\mathcal{H}(t) - \mathcal{H}(0)}{\mathcal{H}(0)}\right|, \tag{4.52}$$

and monitor its value during the simulation to anticipate loss of accuracy.

5. Numerical results

We focus on the case $U = 1$ and $R = 1$, which has dispersion relation (see (2.17))

$$\omega = \pm\sqrt{\frac{E_b(1-\varepsilon)^2}{2(1+\varepsilon)}k^2 - \frac{1}{4}k^2}. \tag{5.1}$$

The critical electric field strength is $E_b^c = (1+\varepsilon)/2(1-\varepsilon)^2$. Throughout this section, we consider three kinds of initial conditions at $t = 0$

$$\theta = -\mu\cos(2\pi\alpha), \quad \varphi = 0, \quad z_0 = -\pi, \qquad \text{for } E_b \geqslant 0; \tag{5.2}$$

$$\theta = -\mu\cos(2\pi\alpha), \quad \varphi = -\mu\left(1 - \frac{2E_b(1-\varepsilon)^2}{(1+\varepsilon)}\right)^{1/2}\sin(2\pi\alpha), \quad z_0 = -\pi, \quad \text{for } 0 \leqslant E_b \leqslant E_b^c; \tag{5.3}$$

$$\theta = -\mu\cos(2\pi\alpha), \quad \varphi = \mu\left(\frac{2E_b(1-\varepsilon)^2}{(1+\varepsilon)} - 1\right)^{1/2}\cos(2\pi\alpha), \quad z_0 = -\pi, \qquad \text{for } E_b \geqslant E_b^c. \tag{5.4}$$

Conditions (5.3) and (5.4) are the eigenmodes of the linearised system: the former represents an exponentially growing mode, while the latter corresponds to a mode travelling at the speed c defined by (3.48). When $E_b = E_b^c$, all three initial conditions are identical. We assume that the Lagrangian markers are uniformly distributed in arclength

https://doi.org/10.1017/jfm.2026.11860 Published online by Cambridge University Press

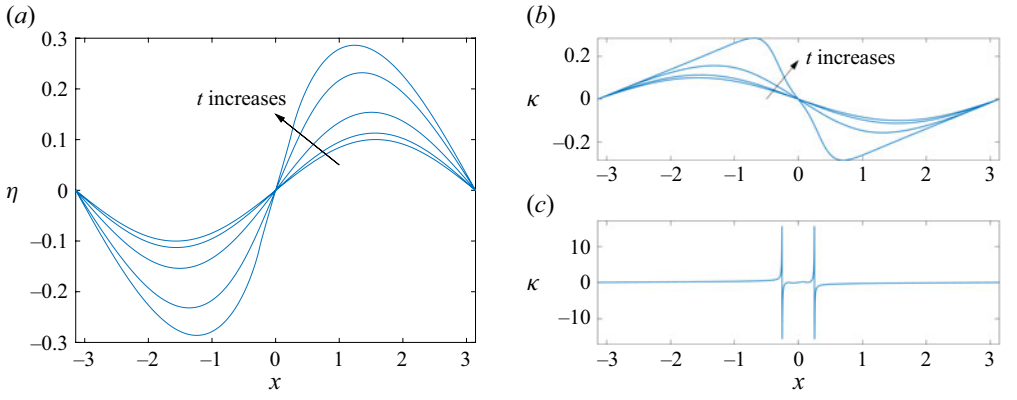


Figure 6. Numerical solutions for $E_b = 0$ and $\mu = 0.1$ with initial condition (5.2). (*a*) Interfaces at $t = 0$, 1, 2, 3 and 3.4925. (*b*) Curvature profiles at $t = 0$, 1, 2, 3. (*c*) Curvature at $t = 3.4925$.

at $t = 0$, thus $s_\alpha(\alpha, 0) = S$, where the total arclength S can be calculated from

$$S = 2\pi \left(\int_0^1 \cos\left(\theta(\alpha, 0)\right) \mathrm{d}\alpha \right)^{-1}. \tag{5.5}$$

When comparing the numerical solutions of the BIM with those of the model equations, we transfer the initial conditions $\theta(\alpha, 0)$ and $\varphi(\alpha, 0)$ to their equivalent conditions for $\eta(x, 0)$ and $\varphi(x, 0)$. This is implemented by first solving a set of non-uniform α values such that the corresponding x-coordinates are uniformly distributed in the x-direction, and then calculating the corresponding values of η.

5.1. *Curvature singularity*

We begin with subcritical values of E_b so that the system is linearly unstable and ill posed due to K–H instability. When $E_b = 0$, we obtain the classical curvature singularity of vortex sheets (Moore 1979; Krasny 1986*b*; Cowley *et al.* 1999), as shown in figure 6 where the initial condition (5.2) was used. The interface and curvature remain odd functions of x during the simulation. They grow and develop the curvature singularity rapidly. Interestingly, the singularity emerges at two symmetrical positions $x = \pm 0.254$, instead of at $x = 0$. This is a typical phenomenon when the initial amplitude is moderate, as reported by Krasny (1986*b*) and Cowley *et al.* (1999).

In figure 7, we show the solution with $E_b = 1$, with initial condition (5.2) as above. The electric field mitigates the K–H instability. The curvature singularity is postponed but eventually develops at $x \approx -0.35$. Note that the odd symmetry of the interface and curvature is broken. In figure 8 we plot the first- and second-order tangential derivatives of the voltage potential V with respect to the arclength. The behaviour is similar to that shown in figure 2, with V_s and V_{ss} developing a local shock and a singularity, respectively, as t_s is approached.

In this section we study the effects of subcritical and supercritical electric fields on curvature singularities. We fix $\varepsilon = 2$, which implies a critical electric field strength $E_b^c = 1.5$. Initial conditions (5.2)–(5.4) are considered with $\mu = 0.1$, which give an almost sinusoidal interface with maximum elevation 0.10014 at $t = 0$.

For other values $E_b < E_b^c$, similar solutions are observed but the time to the singularity increases significantly with E_b. In figure 9, we display typical results for $E_b = 0$, 0.5, 1, 1.3, 1.5 that show the evolution of the L^∞ norm of the curvature. Interestingly,

https://doi.org/10.1017/jfm.2026.11860 Published online by Cambridge University Press

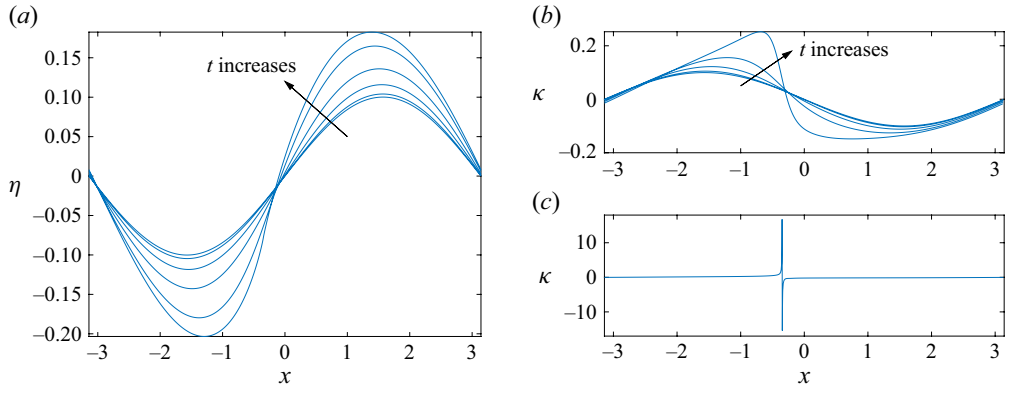


Figure 7. Numerical solutions for $E_b = 1$, $\varepsilon = 2$ and $\mu = 0.1$ with initial condition (5.2). (*a*) Interfaces at $t = 0$, 1, 2, 3, 4 and 4.5. (*b*) Curvature profiles at $t = 0$, 1, 2, 3, 4. (*c*) Curvature at $t = 4.4975$.

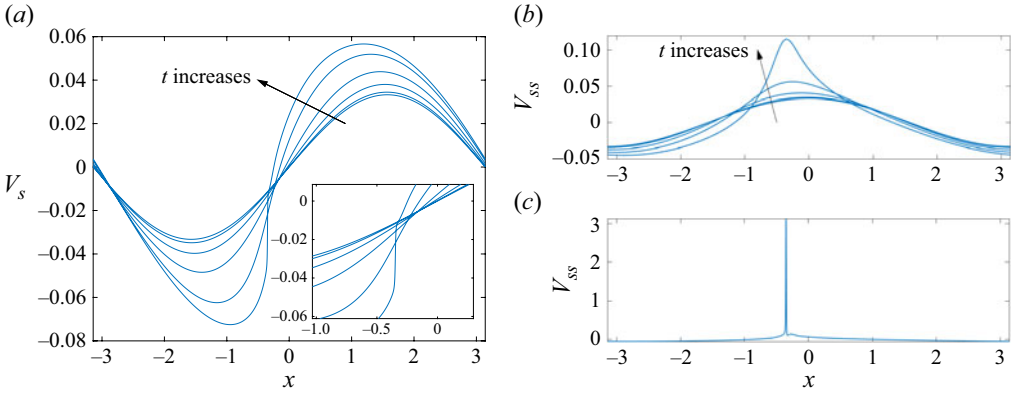


Figure 8. Numerical solutions for $E_b = 1$, $\varepsilon = 2$ and $\mu = 0.1$ with initial condition (5.2): (*a*) V_s at $t = 0$, 1, 2, 3, 4 and 4.5; (*b*) V_{ss} at $t = 0$, 1, 2, 3, 4; (*c*) V_{ss} at $t = 4.4975$.

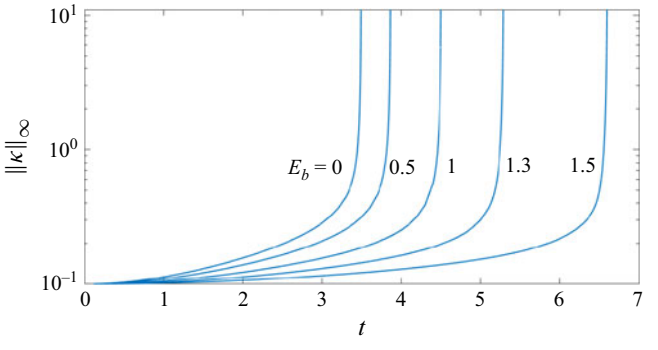


Figure 9. Typical curvature amplitude $\|\kappa\|_\infty$ versus time t for different values of E_b.

when $E_b = E_b^c = 1.5$, a similar growing behaviour of the curvature amplitude is observed, even though linear theory indicates that there is no unstable eigenmode.

For supercritical fields $E_b > E_b^c$ the system becomes neutrally stable and well posed in the linear sense. In figure 10 we set $E_b = 5$ and use the initial condition (5.2). Panels (*a*)

https://doi.org/10.1017/jfm.2026.11860 Published online by Cambridge University Press

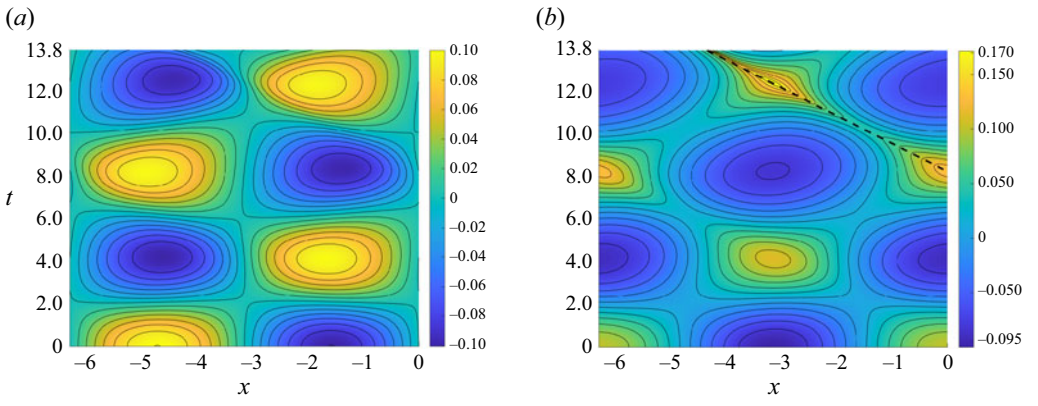


Figure 10. Contour plots of (*a*) η and (*b*) θ for $E_b = 5$, $\varepsilon = 2$ and $\mu = 0.1$ with initial condition (5.2). The dashed line in (*b*) is the characteristic line (5.6).

and (*b*) exhibit contour plots of η and θ, respectively, in the $x-t$ plane. The solution resembles standing waves with an approximate temporal period $2\pi/c = 8.22$, where $c = 0.764$. After one temporal period, the interface develops some visible distortions, but the amplitude is well bounded by its initial value of 0.10014. This demonstrates the stabilising effect of the electric fields. On the other hand, a cusp of θ is gradually formed and propagates leftward at approximately a speed $-c$, consistent with the analysis carried out in § 3 that addressed which component develops the curvature singularity first. In panel (*b*), we plot a typical characteristic line

$$x = -ct + 2\pi, \tag{5.6}$$

which captures well the trajectory of the cusp in the $x - t$ plane.

In figure 11, we compare the results of the full BIM computation (solid curves) with the model (3.13) (dots). Panel (*a*) depicts the interface amplitude of η by evaluating its L^∞ norm $\|\eta\|_\infty$ (this is clearly bounded), and panel (*b*) shows the spatial variation of η at the final computed time $t = 13.88$. Panel (*c*) tracks the evolution of the curvature amplitude $\|\kappa\|_\infty$, which is seen to exhibit oscillatory and growing behaviour, and panel (*d*) shows κ at the final computed time $t = 13.88$, showing the emergence of a curvature singularity. All results demonstrate excellent agreement between the weakly nonlinear model and the fully nonlinear solutions of the Euler-electrostatics equations. Panel (*e*) shows the relative error $\mathcal{H}_r$ of the Hamiltonian (see (4.52) for its definition), which oscillates near round-off level for most of the simulation. Results of the BIM and the model still match well, although a small discrepancy emerges as a singularity is encountered. The structure of the singularity is investigated in panel (*e*) where the spectrum of θ is plotted at successive times as the singularity is approached. The red line indicates an algebraically decaying rate proportional to $k^{-1.5}$, a typical result of the vortex-sheet curvature singularity (Moore 1979; Krasny 1986*b*; Cowley *et al.* 1999).

Figure 12 shows the results for $E_b = 5$ and the initial condition (5.4). Panel (*a*) displays four interfacial solutions at increasing times. The profiles are shifted upwards for comparison. The solid curves, circles and asterisks are results of the BIM, model (3.13) and model (3.52), respectively. The agreement is excellent, with no visible discrepancy. In panel (*b*), we plot the profiles of θ at $t = 14.45$, just before a cusp develops. The discrepancy between the three solutions can now be clearly seen. As explained in § 3.2, given an odd initial condition for η, model (3.52) preserves the odd symmetry with respect to the vertical line $x - ct = 0$. Therefore, the corresponding θ displays even symmetry. On

https://doi.org/10.1017/jfm.2026.11860 Published online by Cambridge University Press

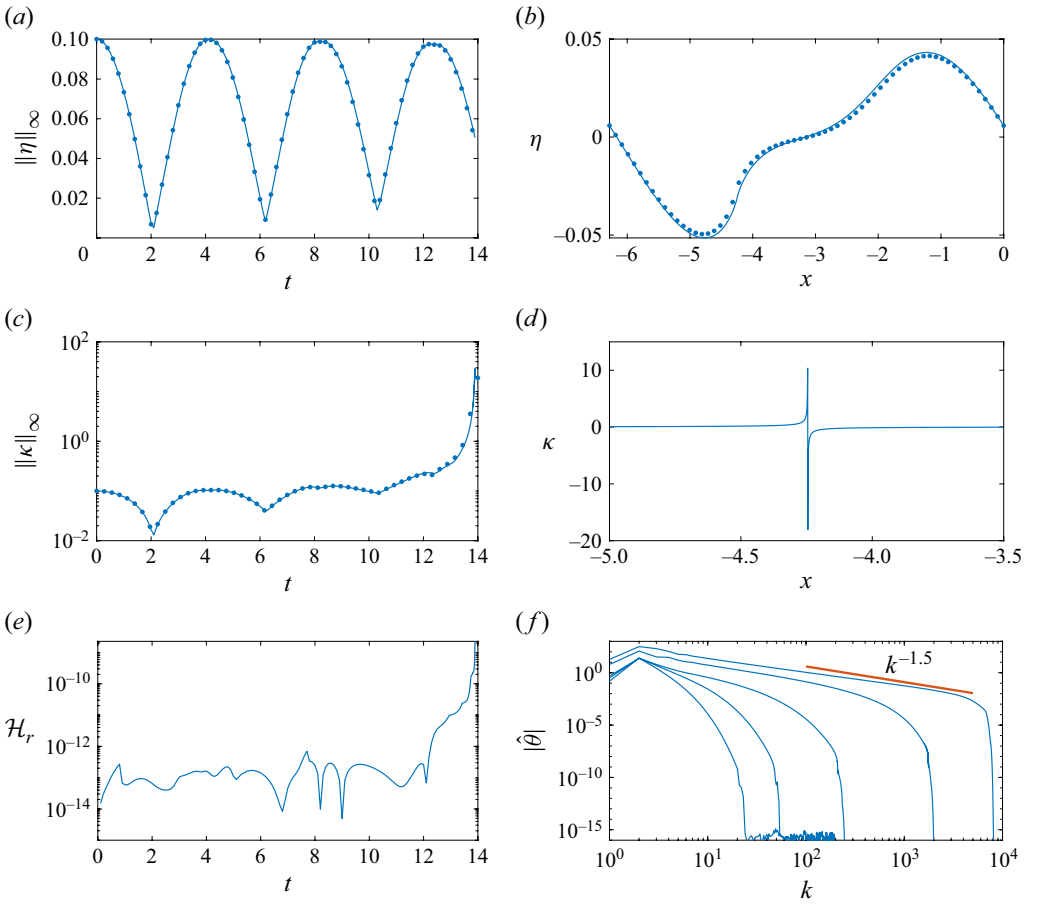


Figure 11. Numerical results for $E_b = 5$, $\varepsilon = 2$ and $\mu = 0.1$ with initial condition (5.2). (*a*) Interface amplitude $\|\eta\|_\infty$ versus t. (*b*) Value of η at $t = 13.88$. (*c*) Curvature amplitude $\|\kappa\|_\infty$ versus time t. (*d*) Local blow-up of κ at $t = 13.88$. (*d*) Relative error of the Hamiltonian $\mathcal{H}_r$. (*e*) Spectrum of θ at $t = 4$, 8, 12, 13.6 and 13.88 from left to right. The red line is proportional to $k^{-1.5}$. In (*a–c*), solid lines and dots are results of the BIM and model (3.13).

the other hand, neither (3.13) nor the full Euler-electrostatics equations have this property. This discrepancy is due to the absence of high-order corrections in (3.52). Nevertheless, (3.52) still provides an excellent estimate of the singularity time t_s, as will be shown in the next subsection. Panel (*c*) plots the curvature amplitude $\|\kappa\|_\infty$ versus time t for the three solutions, exhibiting finite-time blow-up behaviour in all cases. In panel (*d*) we plot the relative error $\mathcal{H}_r$ of the Hamiltonian calculated from the BIM, and we see that it is smaller than 2×10^{-11} throughout the simulation.

5.2. *Singularity time*

In what follows we display some typical numerical results on the singularity time t_s and compare them with the asymptotic estimates obtained in § 3. Note that for the linearised system, the initial conditions (5.3) and (5.4) correspond to a temporally growing eigenmode for subcritical electric fields and a right-travelling eigenmode for supercritical electric fields. They align with the basic assumptions that are used to derive models (3.24) and (3.52). On the other hand, the initial condition (5.2) represents a mixture of growing

https://doi.org/10.1017/jfm.2026.11860 Published online by Cambridge University Press

Range of E_b	Initial conditions			Asymptotic behaviours	
	(5.2)	(5.3)	(5.4)	$\delta \to 0$	$E_b \to \infty$
$E_b < E_b^c$	(3.43)	(3.41)	N/A	$t_s \propto \ln(1/\delta)$	N/A
$E_b > E_b^c$	(3.62)	N/A	(3.59)	$t_s \propto 1/\delta$	$t_s \propto E_b^{-1/2}$

Table 1. Theoretical predictions of the singular time t_s and the asymptotic behaviours for the three initial conditions and different ranges of E_b.

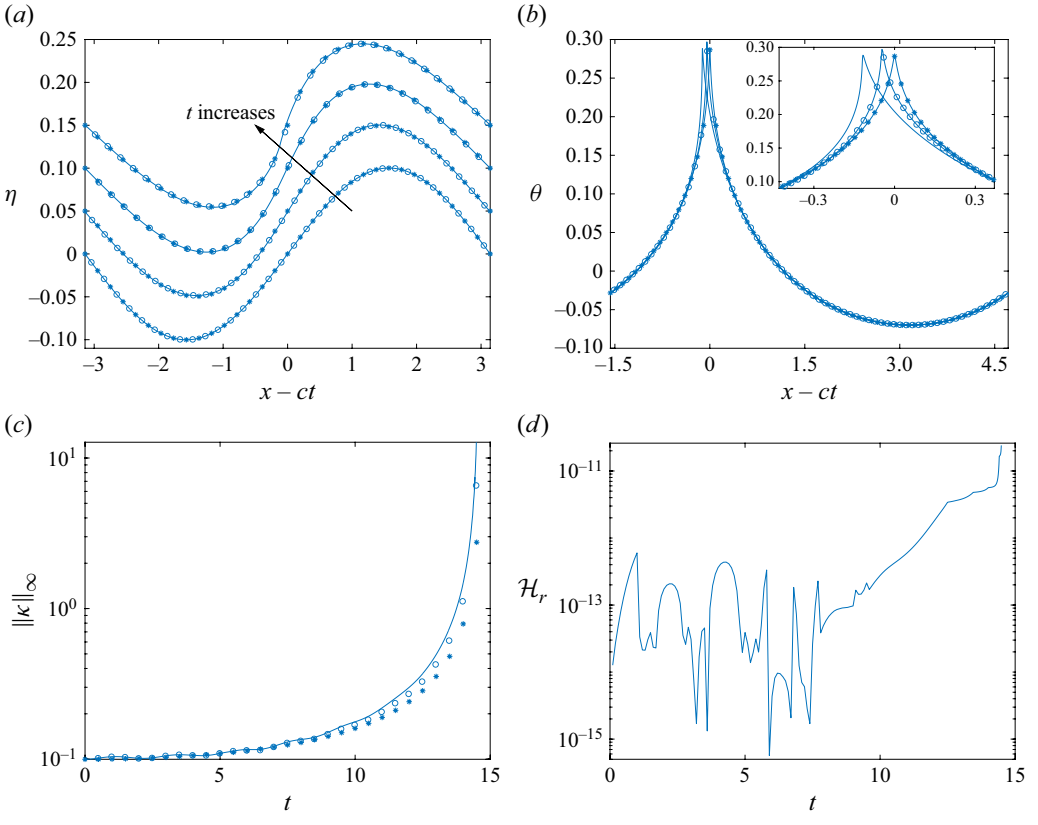


Figure 12. Results for $E_b = 5$ and the initial condition (5.4) in the frame of reference moving at a speed $c = 0.7638$. (*a*) Interfaces at $t = 0$, 5, 10 and 14.45. (*b*) Profiles of θ at $t = 14.45$. (*c*) Curvature amplitude $\|\kappa\|_\infty$ versus time t. (*d*) Relative error $\mathcal{H}_r$ of the Hamiltonian. Solid curves, circles and asterisks represent solutions of BIM, (3.13) and (3.52).

and decaying eigenmodes, or left-travelling and right-travelling eigenmodes. Therefore, the singularity time is dominated by one of these two modes whose initial amplitudes are halved, and the asymptotic estimations remain valid if we replace δ by $\delta/2$, as observed earlier. For convenience, we summarise the theoretical model predictions from § 3 in table 1.

Figure 13 displays some typical results of the variation of t_s with E_b for $\varepsilon = 0.5$. For the parameters used the critical electric field strength is $E_b^c = 3$. Solid curves show results for the four asymptotic predictions represented by their labels, and circles are results obtained from the full BIM simulations with the matched initial conditions shown in table 1. The

https://doi.org/10.1017/jfm.2026.11860 Published online by Cambridge University Press

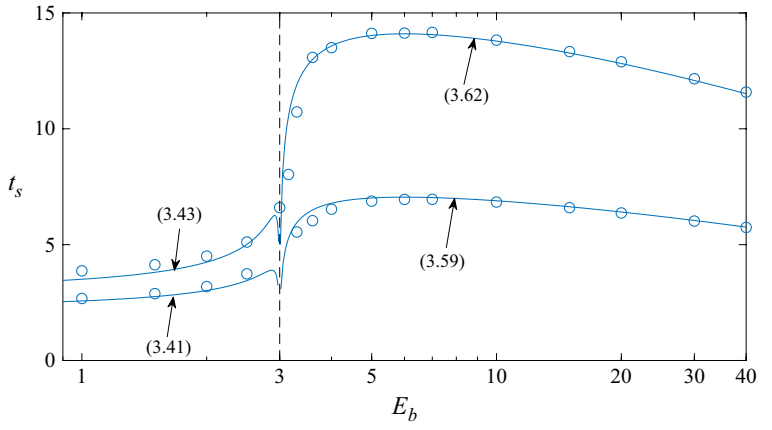


Figure 13. Value of t_s versus E_b obtained from the BIM (circles) and asymptotic estimates (curves) for $\varepsilon = 0.5$. The initial conditions are those matching the theoretical predictions in table 1 with $\mu = 0.1$. The black dashed line identifies the critical electric field strength $E_b^c = 3$.

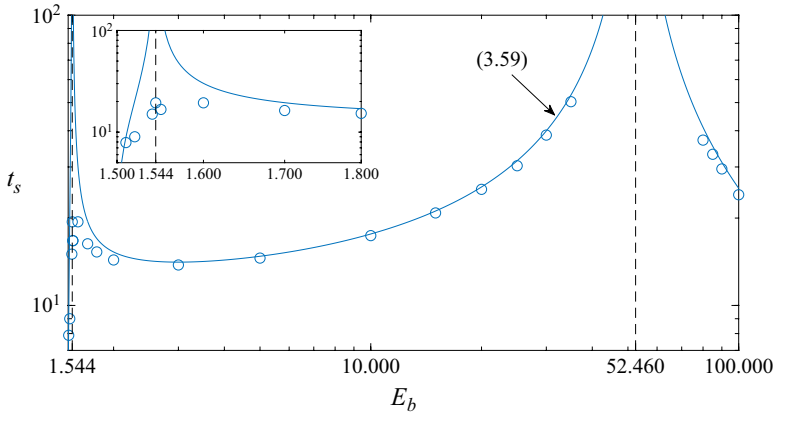


Figure 14. Comparisons of t_s obtained from the BIM (circles) and asymptotic estimates (solid curves) for $\varepsilon = 2$. The initial condition for the BIM is (5.4) with $\mu = 0.1$. The black dashed lines label the two roots, $E_b = 1.544$ and 52.46, of $\gamma = 0$. The corresponding critical electric field strength $E_b^c = 1.5$.

numerical results show that for subcritical values of the electric field, the singularity time t_s increases monotonically with E_b. This behaviour is captured well by the asymptotic estimates (3.41) and (3.43), except in a narrow region adjacent to $E_b = E_b^c = 3$ where a drastic decrease of t_s is predicted. As mentioned previously, this is due to the underlying model (3.24) becoming non-uniformly valid near E_b^c. The numerical results of the BIM simulations (open circles) show that for initial condition (5.2), t_s smoothly increases and passes through the critical line $E_b = E_b^c$. For supercritical electric fields, (3.63) yields that t_s reaches a finite maximum value at $E_b = (1+\varepsilon)/(1-\varepsilon)^2 = 6$, which perfectly matches the numerical results. When $E_b > 6$, t_s slowly decreases with E_b, following the theoretical prediction closely.

When $\varepsilon > 1$, t_s exhibits a totally different behaviour. Figure 14 shows a typical result for $\varepsilon = 2$. The circles represent the results of the BIM simulations for initial condition (5.4) with $\mu = 0.1$, and the solid curves correspond to the asymptotic estimate (3.59).

https://doi.org/10.1017/jfm.2026.11860 Published online by Cambridge University Press

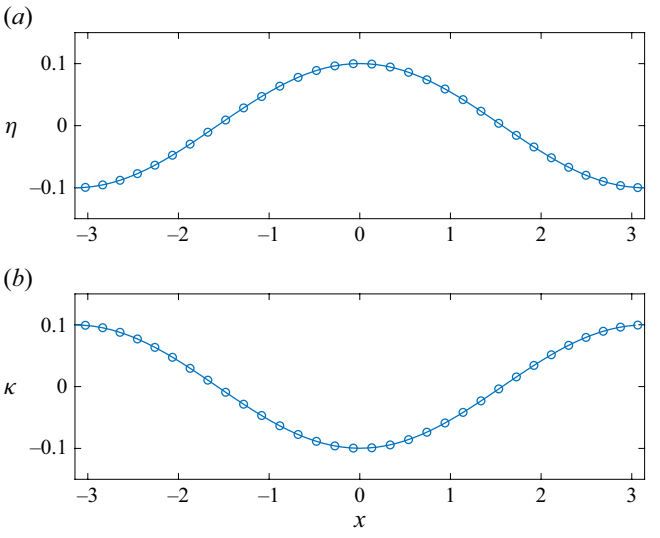


Figure 15. Numerical solutions for $E_b = 52.46$ and $\varepsilon = 2$ at $t = 0$ (curve) and $t = 1000$ (circles). (*a*) Interface η. (*b*) Curvature κ. The solution at $t = 1000$ is shifted along the x-direction for comparison.

Following (3.63), $|\gamma|^{-1}$ blows up at $E_b = 1.544$ and $E_b = 52.46$, suggesting that the curvature singularity is significantly postponed in parameter regions adjacent to these two values. This explains well the observed local peak of t_s around $E_b = 1.544$, even though the full BIM simulation predicts a curvature singularity for $E_b = 1.544$ at $t_s \approx 19.4$. As discussed earlier, the predicted unbounded growth $t_s \to \infty$ by the model (3.24) reflects its breakdown in the vicinity of $E_b = 1.544$. However, it is interesting to note that for solutions centred around $E_b = 52.46$, the corresponding t_s for the full BIM simulations does indeed increase rapidly and follows the theoretical prediction closely. We have not included data for t_s for the full BIM simulations in the interval $E_b \in (35, 80)$, because the curvature singularity develops very slowly and makes the precise estimate of t_s challenging. It is worth mentioning that given small-amplitude initial conditions, solutions for $E_b = 52.46$ are rather stable. Using only 64 Fourier modes, we ran the fully nonlinear simulations up to $t = 1000$ for $\mu = 0.1$ and 0.2 with initial condition (5.4). The spectrum of θ for $\mu = 0.2$ broadens, with the largest amplitude among the last 20 % Fourier modes at $t = 1000$ falling below 10^{-10}, and the amplitude for $\mu = 0.1$ being of the order of round-off level. All solutions exhibit perfect travelling-wave forms. Results for $\mu = 0.1$ are shown in figure 15 where the profiles of the interface and the curvature at $t = 0$ and 1000 (the latter profile is shifted along the x-direction for comparison) are compared.

In the limit $E_b \to \infty$, the asymptotic estimates (3.59) and (3.62) predict that $t_s \propto E_b^{-1/2}$. Figure 16 presents some typical results for $\varepsilon = 0.5$ employing a log–log scale, and using initial condition (5.4) with $\mu = 0.1$. As E_b increases up to 10^4, the computed estimates of t_s show excellent agreement with the theoretical prediction. The numerical results converge to the predicted power law scaling $E_b^{-1/2}$ scaling, which is indicated by the red line.

Finally, we examine the dependence of t_s on the initial amplitude. When $\mu \ll 1$, the initial conditions (5.2)–(5.4) give rise to almost sinusoidal interface profiles with amplitudes nearly equal to μ. For instance, $\mu = 0.1$ corresponds to an almost sinusoidal interface with an amplitude of 0.10014. Therefore, we directly compare our numerical results and the asymptotic estimations without distinguishing μ and δ. In figure 17 we present the numerical results of the BIM simulations and the three model (3.13), (3.24) and

https://doi.org/10.1017/jfm.2026.11860 Published online by Cambridge University Press

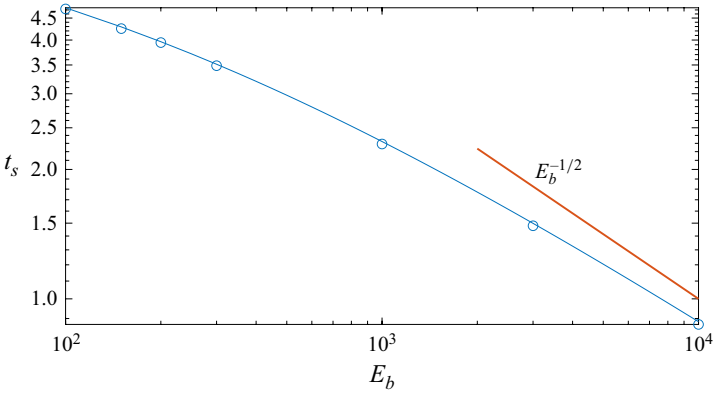


Figure 16. Value of t_s versus E_b in a log–log scale. Circles and curves are results of the BIM and the asymptotic estimation (3.59) for $\varepsilon = 0.5$ and $\mu = 0.1$ with initial condition (5.4). The red line is proportional to $E_b^{-1/2}$.

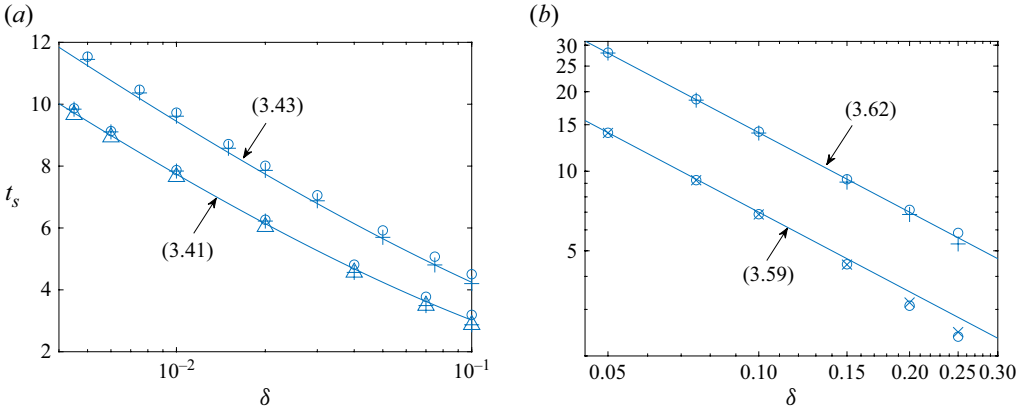


Figure 17. Singular time t_s versus δ for $E_b = 1$, $\varepsilon = 2$ (a), and $E_b = 5$, $\varepsilon = 0.5$ (b). The circles, plus signs, triangles and crosses are numerical results obtained from the BIM simulations, (3.13), (3.24) and (3.52), respectively. The solid curves are theoretical estimates represented by their labels. The initial conditions are those matching the theoretical predictions in table 1.

(3.52). The results for each are represented by the circles, plus signs, triangles and crosses, respectively. The solid curves are theoretical predictions corresponding to their labels. The initial conditions are those matched in table 1, and they are numerically transformed into the initial conditions for η and φ when solving the model equations, as explained in § 5. In figure 17(a) we set $E_b = 1$ and $\varepsilon = 2$ (subcritical electric field). The t_s values obtained from the BIM simulations and the various model equations agree well and follow the theoretical predictions consistently. Figure 17(b) displays results for $E_b = 5$ and $\varepsilon = 0.5$ (supercritical TEF) using a log–log scale. The numerical results exhibit a clear inverse proportionality with δ, and match the theoretical predictions precisely when $\delta < 0.1$. For moderate values of δ, nonlinear effects cause t_s to slightly deviate from the theoretical predictions, with an underestimation for (3.59) and an overestimation of (3.62).

https://doi.org/10.1017/jfm.2026.11860 Published online by Cambridge University Press

6. Conclusions

In this paper we investigated the nonlinear evolution of electrified vortex sheets and addressed computationally the question of existence of large time solutions starting from smooth initial conditions. Our study is motivated by the observations that strong TEFs can suppress the K–H instability in the linear regime, hence suggesting that the electrified vortex sheet might arrest the finite-time curvature singularity encountered in non-electrified vortex sheets. The electric field acts as a regularisation mechanism that has not been studied in detail. We undertake both theoretical and computational approaches. For small-amplitude initial perturbations, linear stability analysis shows that the system undergoes a transition from an unstable regime, to a neutrally stable regime and then an unstable regime when the electric field strength E_b exceeds a critical value E_b^c. This suggests that electrified vortex sheets would have very different behaviour in the subcritical regime $E_b < E_b^c$, and the supercritical regime $E_b > E_b^c$.

To derive leading-order reduced-dimension evolution equations, we take advantage of the Hamiltonian formulation that has been widely used in studies of water waves and interfacial waves (Zakharov 1968; Benjamin & Bridges 1997; Guan & Wang 2022; Wang 2022). By using the Craig–Sulem recursion relation of the DNOs (Craig & Sulem 1993), we obtain three quadratic weakly nonlinear models: these are model (3.24) that applies in the subcritical regime, model (3.52) valid in the supercritical regime and model (3.13) that applies for general cases. As far as we know these models are new and provide alternative approaches to the study of vortex sheets (electrified or not) to be compared with models proposed by Caflisch & Semmes (1990), for example. In particular, model (3.24) is similar to the Constantin–Lax–Majda equation (Constantin *et al.* 1985) when $E_b = 0$, but is derived from a physical problem from first principles rather than proposed phenomenologically.

In addition to analysis and computations of model equations, we propose a time-dependent BIM to simulate the fully nonlinear evolution of the electrified vortex sheets governed by the Euler-electrostatic equations. Our numerical scheme uses Cauchy's integral formula to solve Laplace's equation, and the $\theta - s_\alpha$ formulation (Yang 1992; Hou *et al.* 1994; Guan & Vanden-Broeck 2025) to track the interface. Following Grue *et al.* (1997), we apply a Lagrangian framework by introducing artificial fluid markers on the interface. This is particularly efficient when curvature singularities develop because the accumulation of fluid markers significantly enhances the physical resolution.

For small-amplitude sinusoidal initial conditions, we observe finite-time curvature singularities for the model equations and the fully nonlinear BIM simulations, regardless of the strength of the TEFs. In the subcritical regime, the singularity is the counterpart of the Moore singularity found in the classical vortex-sheet problem (Moore 1979), with the difference that the odd parity of the solutions is broken by the electric field. Meanwhile, the first-order derivative of the voltage potential, i.e. the tangential component of the electric field, develops a shock at the same position as the curvature singularity. To estimate the singularity time t_s, we perform Moore's analysis to model (3.24) and find that $t_s \propto \ln(1/\delta)$ for $\delta \ll 1$, where δ is the initial amplitude of the perturbation to a flat vortex sheet. Interestingly, our result degenerates to Moore's classical result when $E_b = 0$. For fixed δ, the full BIM simulations suggest that t_s monotonically increases with E_b until entering the supercritical regime. This behaviour is captured well by the theoretical estimates of t_s given by (3.41) and (3.43), except when $E_b \to E_b^c$ when the model (3.24) breaks down.

In the supercritical regime, solutions resemble standing waves or travelling waves, depending on the specific form of the initial condition, but curvature singularities

https://doi.org/10.1017/jfm.2026.11860 Published online by Cambridge University Press

eventually appear, albeit at possibly large times. The quadratic nonlinear model (3.52) captures this singular behaviour well, although some small discrepancies with the full BIM solutions are observed, most likely due to the lack of high-order corrections in the models. In addition, the model (3.52) yields that $t_s \propto 1/\delta$ for $\delta \ll 1$, and this matches the numerical results remarkably well. For fixed δ, the theoretical estimates (3.59) and (3.62) show that t_s follows two types of behaviour: (i) for $cU(\varepsilon - 1) < 0$, t_s reaches a finite maximum; (ii) for $cU(\varepsilon - 1) > 0$, t_s becomes infinite when E_b takes on two special values that we can determine analytically. We find that case (i) matches the full BIM solutions very well. For case (ii), when E_b takes on the larger of the special predicted values the solutions become rather stable and longer lived, while for the other smaller special value the evolution leads to a curvature singularity in moderate time. A possible explanation for this is that when E_b is close to these special values the cubic nonlinearity becomes equally important as the quadratic nonlinearity retained in the models, leading to the possibility of singularity formation in finite time. When $E_b \to \infty$, both theoretical predictions and the fully nonlinear simulations suggest that $t_s \propto E_b^{-1/2}$.

The current work did not consider the effects of gravity and surface tension. It would be interesting to couple these physical mechanisms with an electric field and investigate how they influence the vortex sheet. Some of our preliminary results show that the curvature singularity is replaced by the pinching singularity, similar to those reported in Hou *et al.* (1994, 1997). The simulations can also be extended to the finite-depth case. It is not clear whether there is curvature singularity or the touch-down singularity found by Gao *et al.* (2024). For models (3.24) and (3.52), extensions to include cubic nonlinearities when $E_b = E_b^c$ or the values leading to t_s blow up, are necessary. This might give some clues to understand the robust solutions that we observed.

Funding. X.G. was supported by a Chapman Fellowship, Department of Mathematics, Imperial College London. The work of D.T.P. was partly supported by CBET-EPSRC grant EP/V062298/1.

Declaration of interests. The authors report no conflict of interest.

Data availability statement. Data available on request from the authors.

Appendix A. Linear dispersion relation and physical mechanism of electrostatic stabilisation

After linearising the boundary conditions (2.14) and (2.16), we have

$$\begin{cases} \eta_t + \dfrac{U}{2}\eta_x - \phi_{1,y} = 0, \\ \eta_t - \dfrac{U}{2}\eta_x - \phi_{2,y} = 0, \\ \phi_{1,t} + \dfrac{U}{2}\phi_{1,x} + \dfrac{\eta}{F_r^2} - R\left(\phi_{2,t} - \dfrac{U}{2}\phi_{2,x} + \dfrac{\eta}{F_r^2}\right) + E_b\left(\varepsilon V_{2,x} - V_{1,x}\right) = 0, \\ V_1 - V_2 = 0, \\ V_{1,y} - \varepsilon V_{2,y} - (1-\varepsilon)\eta_x = 0. \end{cases} \tag{A1}$$

Assuming that

$$(\eta, \phi_1, \phi_2, V_1, V_2) = \mathrm{e}^{i(kx-\omega t)}(\tilde{\eta}, \mathrm{e}^{|k|y}\tilde{\phi}_1, \mathrm{e}^{-|k|y}\tilde{\phi}_2, \mathrm{e}^{|k|y}\tilde{V}_1, \mathrm{e}^{-|k|y}\tilde{V}_2) + \text{c.c.}, \tag{A2}$$

https://doi.org/10.1017/jfm.2026.11860 Published online by Cambridge University Press

where c.c. denotes complex conjugate and $\tilde{\eta}, \tilde{\phi}_1, \tilde{\phi}_2, \tilde{V}_1$ and $\tilde{V}_2$ are small constant coefficients. Substituting (A2) into (A1), we arrive at the following homogeneous linear equations:

$$\begin{bmatrix} -\mathrm{i}\omega_1 & -|k| & 0 & 0 & 0 \\ -\mathrm{i}\omega_2 & 0 & |k| & 0 & 0 \\ 0 & 0 & 0 & 1 & -1 \\ -\mathrm{i}k(1-\varepsilon) & 0 & 0 & |k| & |k|\varepsilon \\ (1-R)/F_r^2 & -\mathrm{i}\omega_1 & \mathrm{i}R\omega_2 & -\mathrm{i}kE_b & \mathrm{i}kE_b\varepsilon \end{bmatrix} \begin{bmatrix} \tilde{\eta} \\ \tilde{\phi}_1 \\ \tilde{\phi}_2 \\ \tilde{V}_1 \\ \tilde{V}_2 \end{bmatrix} = \begin{bmatrix} 0 \\ 0 \\ 0 \\ 0 \\ 0 \end{bmatrix}, \tag{A3}$$

where $\omega_i = \omega + (-1)^i kU/2$, $(i = 1, 2)$. This gives the following linear solution:

$$\tilde{\phi}_1 = -\frac{\mathrm{i}\omega_1}{|k|}\tilde{\eta}, \quad \tilde{\phi}_2 = \frac{\mathrm{i}\omega_2}{|k|}\tilde{\eta}, \quad \tilde{V}_1 = \tilde{V}_2 = \mathrm{i}\,\mathrm{sgn}(k)\frac{1-\varepsilon}{1+\varepsilon}\tilde{\eta}. \tag{A4}$$

The solvability condition of (A3) gives rise to the following quadratic equation for ω:

$$\mathcal{A}\omega^2 - \mathcal{B}\omega + \mathcal{C} = 0, \tag{A5}$$

where

$$\mathcal{A} = (1+\varepsilon)(1+R), \tag{A6}$$

$$\mathcal{B} = kU(1+\varepsilon)(1-R), \tag{A7}$$

$$\mathcal{C} = k^2(1+\varepsilon)(1+R)/4 - |k|(1-R)(1+\varepsilon)/F_r^2 - k^2E_b(1-\varepsilon)^2. \tag{A8}$$

Solving (A5), we obtain the following dispersion relation:

$$\omega = \frac{U(1-R)}{2(1+R)}k \pm \sqrt{\frac{1-R}{(1+R)F_r^2}|k| + \frac{E_b(1-\varepsilon)^2}{(1+\varepsilon)(1+R)}k^2 - \frac{R}{(1+R)^2}k^2}. \tag{A9}$$

We consider next the mechanism of linear stabilisation by a horizontal electric field. Given a small interfacial perturbation $\eta = \delta\cos(kx)$, we can calculate the electric force normal to the interface from the formula

$$f_e = -\big[\boldsymbol{n}\cdot\boldsymbol{\Sigma}\cdot\boldsymbol{n}\big]_2^1, \tag{A10}$$

where $\boldsymbol{\Sigma}$ is the electrostatic Maxwell stress tensor, and $\boldsymbol{n}$ represents the unit normal pointing into fluid 2 (dimensional variables are used). Consequently, a positive f_e corresponds to a net force on the interface pointing into fluid 2. Using the linear solution detailed above, we have

$$f_e \approx \frac{\varepsilon_2-\varepsilon_1}{2}E_0^2 - \delta\frac{(\varepsilon_2-\varepsilon_1)^2}{\varepsilon_2+\varepsilon_1}E_0^2|k|\cos(kx) = \frac{\varepsilon_2-\varepsilon_1}{2}E_0^2 - \frac{(\varepsilon_2-\varepsilon_1)^2}{\varepsilon_2+\varepsilon_1}E_0^2|k|\eta. \tag{A11}$$

The first term on the right-hand side of (A11) represents a constant electrostatic pressure jump across the flat interface and has no influence on linear stability. The second term is proportional to the interfacial displacement and underpins the linear stability characteristics. Since the fluctuating part of f_e in (A11) is proportional to $-\eta$, i.e. is out of phase, it follows that it induces a restoring force which tends to suppress the growth of perturbation due to the K–H instability. Figure 18 shows an illustration of this electric force stabilisation mechanism.

We can conclude that the stabilising effect of horizontal electric fields is similar to that due to surface tension, but there are two important distinctions: first, surface tension

https://doi.org/10.1017/jfm.2026.11860 Published online by Cambridge University Press

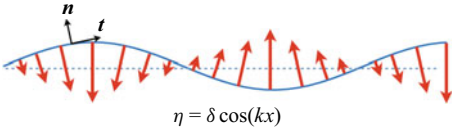


Figure 18. An illustration of the electric force due to an interface perturbation.

generates a restoring force proportional to $k^2\eta$, so it is more pronounced for short waves compared with the electric force. Second, the effect of surface tension is local because it only depends on curvature. On the other hand, the electric force depends on the interface displacement η and the voltage potential V globally because it involves $\partial V_{1,2}/\partial \boldsymbol{n}$ which must be obtained by solving Laplace's equation.

Appendix B. The Hamiltonian structure

Following § 3, the Hamiltonian is written as

$$\mathcal{H} = \frac{1}{2}\int \varphi_1 G^- \varphi_1 \,\mathrm{d}x + \frac{R}{2}\int \varphi_2 G^+ \varphi_2 \,\mathrm{d}x - \frac{U}{2}\int \varphi_1 \eta_x \,\mathrm{d}x - \frac{RU}{2}\int \varphi_2 \eta_x \,\mathrm{d}x + \frac{E_b}{2}\int V\left(G^- V + \varepsilon G^+ V\right)\mathrm{d}x + \frac{1-R}{2F_r^2}\int \eta^2 \,\mathrm{d}x, \tag{B1}$$

where we have omitted the upper and lower limits of the integration, and suppressed the dependence of $G^{\pm}$ on η, for convenience. To express $\mathcal{H}$ in terms of η and φ, we first rewrite the kinematic boundary condition as

$$\begin{cases} \eta_t + \dfrac{U}{2}\eta_x = G^- \varphi_1, \\ \eta_t - \dfrac{U}{2}\eta_x = -G^+ \varphi_2. \end{cases} \tag{B2}$$

Eliminating η, we get the following identity:

$$G^- \varphi_1 + G^+ \varphi_2 = U\eta_x. \tag{B3}$$

Since $\varphi = \varphi_1 - R\varphi_2$, (B3) is equivalent to

$$G^-(\varphi + R\varphi_2) + G^+\varphi_2 = U\eta_x, \tag{B4}$$

$$RG^-\varphi_1 + G^+(\varphi_1 - \varphi) = RU\eta_x. \tag{B5}$$

Therefore, φ_1 and φ_2 can be expressed as

$$\varphi_1 = (G^+ + RG^-)^{-1}(G^+\varphi + RU\eta_x), \tag{B6}$$

$$\varphi_2 = (G^+ + RG^-)^{-1}(U\eta_x - G^-\varphi). \tag{B7}$$

https://doi.org/10.1017/jfm.2026.11860 Published online by Cambridge University Press

Using (B3), (B6) and (B7), the first line of (B1) becomes

$$\begin{aligned}
&\frac{1}{2}\int \varphi_1 G^- \varphi_1 \,\mathrm{d}x + \frac{R}{2}\int \varphi_2 (U\eta_x - G^-\varphi_1)\,\mathrm{d}x - \frac{U}{2}\int \varphi_1\eta_x \,\mathrm{d}x - \frac{RU}{2}\int \varphi_2\eta_x \,\mathrm{d}x \\
&= \frac{1}{2}\int \varphi G^-(G^+ + RG^-)^{-1}G^+\varphi \,\mathrm{d}x - \frac{U}{2}\int \eta_x\varphi \,\mathrm{d}x + RU\int \eta_x(G^+ + RG^-)^{-1}G^-\varphi \,\mathrm{d}x \\
&- \frac{R}{2}\int \eta_x(G^+ + RG^-)^{-1}\eta_x \,\mathrm{d}x \\
&= \frac{1}{2}\int \varphi G^-(G^+ + RG^-)^{-1}G^+\varphi \,\mathrm{d}x - \frac{U}{2}\int \eta_x(G^+ + RG^-)^{-1}(G^+ - RG^-)\varphi \,\mathrm{d}x \\
&- \frac{R}{2}\int \eta_x(G^+ + RG^-)^{-1}\eta_x \,\mathrm{d}x,
\end{aligned} \tag{B8}$$

where we have used the fact that G^- and G^+ are self-adjoint operators, and consequently so is $(G^+ + RG^-)^{-1}$. To simplify the second line of (B1), we use the condition (2.10)

$$(G^- + \varepsilon G^+)V = (1-\varepsilon)\eta_x. \tag{B9}$$

Ultimately, we obtain the following form of the Hamiltonian:

$$\begin{aligned}
\mathcal{H} = &\frac{1}{2}\int \varphi G^-(G^+ + RG^-)^{-1}G^+\varphi \,\mathrm{d}x - \frac{U}{2}\int \eta_x(G^+ + RG^-)^{-1}(G^+ - RG^-)\varphi \,\mathrm{d}x \\
&- \frac{R}{2}\int \eta_x(G^+ + RG^-)^{-1}\eta_x \,\mathrm{d}x + \frac{E_b(1-\varepsilon)^2}{2}\int \eta_x(G^- + \varepsilon G^+)^{-1}\eta_x \,\mathrm{d}x + \frac{1-R}{2F_r^2}\int \eta^2 \,\mathrm{d}x.
\end{aligned} \tag{B10}$$

When $\eta \ll 1$, G^- and G^+ have convergent Taylor series

$$G^- = \sum_{n=0}^{\infty} G_n, \quad G^+ = \sum_{n=0}^{\infty} (-1)^n G_n. \tag{B11}$$

The first two terms are

$$G_0 = (-\partial_{xx})^{1/2}, \tag{B12}$$

$$G_1 = -G_0\eta G_0 - \partial_x \eta \partial_x. \tag{B13}$$

The composite operators in (B1) can be expanded asymptotically. For instance, the operator $(G^+ + RG^-)^{-1}$ can be expanded as

$$\begin{aligned}
(G^+ + RG^-)^{-1} &= \left[(1+R)G_0\left(1 - \frac{1-R}{1+R}G_0^{-1}G_1 + \cdots\right)\right]^{-1} \\
&= \frac{G_0^{-1}}{1+R} - \frac{1-R}{(1+R)^2}\left(\eta + \partial_x G_0^{-1}\eta G_0^{-1}\partial_x\right) + \cdots.
\end{aligned} \tag{B14}$$

This allows us to truncate the Hamiltonian to any desired order.

Appendix C. Moore's analysis

For (3.24), we write its solutions in the form of Fourier series

$$\eta(x,t) = \sum_{m=-\infty}^{\infty} \underbrace{\delta^{|m|}\mathrm{e}^{\lambda|m|t}A_m(t)}_{a_m(t)}\,\mathrm{e}^{imx}. \tag{C1}$$

https://doi.org/10.1017/jfm.2026.11860 Published online by Cambridge University Press

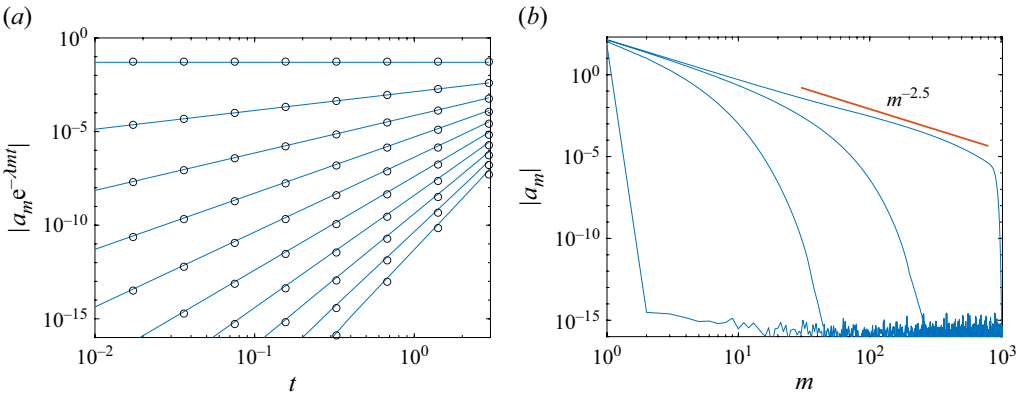


Figure 19. Numerical results of (3.24) with $U = 1$, $E_b = 1$, $\varepsilon = 2$ and initial condition $\eta(x, 0) = 0.1\sin(x)$: (*a*) $|a_m e^{-\lambda m t}|$ versus $t \in [0, 2.932]$ in a log–log scale. From top to bottom, m ranges from 1 to 10. The solid lines and circles are results from the model equation and the asymptotic estimate (C17); (*b*) a_m at $t = 0$, 2, 2.8 and 2.932 from left to right. The red straight line is proportional to $m^{-2.5}$.

The initial condition

$$\eta(x, 0) = \delta \sin(x), \tag{C2}$$

implies that

$$A_m(0) = \begin{cases} -\dfrac{\mathrm{i}}{2}, & \text{if } m = 1; \\ \dfrac{\mathrm{i}}{2}, & \text{if } m = -1; \\ 0, & \text{otherwise.} \end{cases} \tag{C3}$$

Since η is a real-valued function, we only need to consider the case $m > 0$. Substituting (C1) into (3.24) and collecting the $O(\delta^{|m|})$ terms, we have

$$\frac{\mathrm{d}A_m}{\mathrm{d}t} \sim \mathrm{i}\frac{U}{2}\sum_{n=0}^{m}|n|(m-n)A_{m-n}A_n + \frac{E_b(1-\varepsilon)^3}{8\lambda(1+\varepsilon)^2}\Bigg[\sum_{n=0}^{m}2|m||n|A_{m-n}A_n + \sum_{n=0}^{m}|m-n||n|A_{m-n}A_n - \sum_{n=0}^{m}(m-n)nA_{m-n}A_n - 2\sum_{n=0}^{m}n^2A_{m-n}A_n\Bigg]. \tag{C4}$$

Note that other terms ignored in the infinite sum are assumed to be secondary important, provided that $\lambda t < \ln(1/\delta)$. By taking the leading order of (C4), we have

$$A_m(t) \sim B_m t^{m-1}. \tag{C5}$$

Numerical evidence supporting (C5) is shown in figure 19(*a*). Note that (C5) implies that the asymptotic expansion (C1) is uniformly valid provided $t = o(1/\delta)$. Assuming this is true for a moment (its legitimacy will be confirmed *a posteriori*), we get an algebraic equation for B_m

$$(m-1)B_m = J\sum_{n=1}^{m-1}(m-n)nB_{m-n}B_n, \tag{C6}$$

https://doi.org/10.1017/jfm.2026.11860 Published online by Cambridge University Press

where

$$J = \mathrm{i}\frac{U}{2} + \frac{E_b(1-\varepsilon)^3}{4\lambda(1+\varepsilon)^2}. \tag{C7}$$

Following Moore (1979), we introduce a generating function $g(x)$

$$g(x) = B_1 x + B_2 x^2 + B_3 x^3 + \cdots, \tag{C8}$$

where $B_1 = -\mathrm{i}/2$, according to (C3). Equation (C6) is equivalent to the following ordinary differential equation:

$$\frac{d}{\mathrm{d}x}\left(\frac{g}{x}\right) = J\left(\frac{\mathrm{d}g}{\mathrm{d}x}\right)^2. \tag{C9}$$

An implicit solution is

$$\begin{cases} g(v) = \dfrac{1}{2J}\left(v - \dfrac{v^2}{2}\right), \\ x(v) = \dfrac{\mathrm{i}}{J} v\mathrm{e}^{-v}. \end{cases} \tag{C10}$$

Since $x'(v) = 0$ at $v = 1$, this is the only branch point. According to Darboux's method, the asymptotic behaviour of B_m can be obtained by seeking the Maclaurin expansion of the leading singular term of g. Introducing

$$d = 1 + \mathrm{i}J\mathrm{e}x = 1 - v\mathrm{e}^{1-v}, \tag{C11}$$

it is straightforward to show that

$$v \sim 1 - \sqrt{2d} + \frac{2}{3}d - \frac{5\sqrt{2}}{9}d^{3/2} + \cdots, \quad \text{as} \quad d \to 0. \tag{C12}$$

As a result

$$g \sim \frac{1}{2J}\left(\frac{1}{2} - d + \frac{2\sqrt{2}}{3}d^{3/2} + \cdots\right), \quad \text{as} \quad d \to 0. \tag{C13}$$

Assuming the leading singular term has Maclaurin expansion

$$\frac{\sqrt{2}}{3J}(1 + \mathrm{i}J\mathrm{e}x)^{3/2} = \sum_{m=1}^{\infty} b_m x^m, \tag{C14}$$

Darboux's method suggests that

$$B_m \sim b_m, \quad \text{as} \quad m \to \infty. \tag{C15}$$

Using the binomial theorem and the gamma function, we have

$$B_m \sim \frac{1}{2\sqrt{2\pi}\,J}(-\mathrm{i}J\mathrm{e})^m m^{-5/2}, \quad \text{as} \quad m \to \infty, \tag{C16}$$

and consequently

$$a_m(t) \sim \frac{1}{2\sqrt{2\pi}\,J} m^{-5/2} \mathrm{e}^{m\left(1+\lambda t + \ln t + \ln(-iJ) + \ln\delta\right)}. \tag{C17}$$

https://doi.org/10.1017/jfm.2026.11860 Published online by Cambridge University Press

Since t_s is defined as the moment that a_m loses its exponential decay rate with m, and

$$\mathrm{Re}\big\{\ln(-\mathrm{i}J)\big\} = \frac{1}{2}\ln\left(\frac{1}{4} + \left(\frac{E_b(1-\varepsilon)^3}{4\lambda(1+\varepsilon)^2}\right)^2\right), \tag{C18}$$

we obtain the following equation for t_s:

$$1 + \lambda t_s + \ln t_s + \ln\delta + \frac{1}{2}\ln\left(\frac{1}{4} + \left(\frac{E_b(1-\varepsilon)^3}{4\lambda(1+\varepsilon)^2}\right)^2\right) = 0. \tag{C19}$$

Figure 19 compares the numerical results of (3.24) with $U = 1$, $E_b = 1$, $\varepsilon = 2$ and the initial condition $\eta(x, 0) = 0.1\sin(x)$. In panel (a), the solid curves are the temporal evolution of $|a_m \mathrm{e}^{-\lambda m t}|$ for $m = 1, 2, \cdots, 10$. The circles are from the asymptotic relation (C17). The results are plotted in a log–log scale to clearly show that the relation (C5) is accurate. In panel (b), we plot the Fourier coefficients a_m at $t = 0$, 2, 2.8 and 2.932 from left to right. The red straight line is proportional to $m^{-5/2}$, which matches the final spectrum very well. According to (C19), the singularity time $t_s = 3.02$.

References

Ambrose, D.M., Camassa, R., Marzuola, J.L., McLaughlin, R.M., Robinson, Q. & Wilkening, J. 2022 Numerical algorithms for water waves with background flow over obstacles and topography. *Adv. Comput. Maths* **48** (4), 46.

Anderson, T.G., Cimpeanu, R., Papageorgiou, D.T. & Petropoulos, P.G. 2017 Electric field stabilization of viscous liquid layers coating the underside of a surface. *Phys. Rev. Fluids* **2** (5), 054001.

Baker, G., Caflisch, R.E. & Siegel, M. 1993 Singularity formation during Rayleigh–Taylor instability. *J. Fluid Mech.* **252**, 51–78.

Baker, G. & Nachbin, A. 1998 Stable methods for vortex sheet motion in the presence of surface tension. *SIAM J. Sci. Comput.* **19** (5), 1737–1766.

Baker, G.R., Meiron, D.I. & Orszag, S.A. 1982 Generalized vortex methods for free-surface flow problems. *J. Fluid Mech.* **123**, 477–501.

Baker, G.R. & Shelley, M.J. 1990 On the connection between thin vortex layers and vortex sheets. *J. Fluid Mech.* **215**, 161–194.

Barannyk, L.L., Papageorgiou, D.T. & Petropoulos, P.G. 2012 Suppression of Rayleigh–Taylor instability using electric fields. *Maths Comput. Simul.* **82** (6), 1008–1016.

Barannyk, L.L., Papageorgiou, D.T., Petropoulos, P.G. & Vanden-Broeck, J.-M. 2015 Nonlinear dynamics and wall touch-up in unstably stratified multilayer flows in horizontal channels under the action of electric fields. *SIAM J. Appl. Maths* **75** (1), 92–113.

Benjamin, T.B. & Bridges, T.J. 1997 Reappraisal of the Kelvin–Helmholtz problem. Part 1. Hamiltonian structure. *J. Fluid Mech.* **333**, 301–325.

Caflisch, R.E. & Orellana, O.F. 1986 Long time existence for a slightly perturbed vortex sheet. *Commun. Pure Appl. Maths* **39** (6), 807–838.

Caflisch, R.E. & Orellana, O.F. 1989 Singular solutions and ill-posedness for the evolution of vortex sheets. *SIAM J. Math. Anal.* **20** (2), 293–307.

Caflisch, R.E., Orellana, O.F. & Siegel, M. 1990 A localized approximation method for vortical flows. *SIAM J. Appl. Maths* **50** (6), 1517–1532.

Caflisch, R.E. & Semmes, S. 1990 A nonlinear approximation for vortex sheet evolution and singularity formation. *Phys. D* **41** (2), 197–207.

Cimpeanu, R., Papageorgiou, D.T. & Petropoulos, P.G. 2014 On the control and suppression of the Rayleigh–Taylor instability using electric fields. *Phys. Fluids* **26** (2), 022105.

Coifman, R. & Meyer, Y. 1985 Nonlinear harmonic analysis and analytic dependence. *Pseudodifferential Operators Applics* **43** (71–78), 12.

Constantin, P., Lax, P.D. & Majda, A. 1985 A simple one-dimensional model for the three-dimensional vorticity equation. *Commun. Pure Appl. Maths* **38** (6), 715–724.

Cowley, S.J., Baker, G.R. & Tanveer, S. 1999 On the formation of Moore curvature singularities in vortex sheets. *J. Fluid Mech.* **378**, 233–267.

https://doi.org/10.1017/jfm.2026.11860 Published online by Cambridge University Press

CRAIG, W. & GROVES, M.D. 1994 Hamiltonian long-wave approximations to the water-wave problem. *Wave Motion* **19** (4), 367–389.

CRAIG, W., GUYENNE, P. & SULEM, C. 2012 The surface signature of internal waves. *J. Fluid Mech.* **710**, 277–303.

CRAIG, W. & SULEM, C. 1993 Numerical simulation of gravity waves. *J. Comput. Phys.* **108** (1), 73–83.

DOLD, J.W. 1992 An efficient surface-integral algorithm applied to unsteady gravity waves. *J. Comput. Phys.* **103** (1), 90–115.

DOLD, J.W. & PEREGRINE, D.H. 1986 An efficient boundary-integral method for steep unsteady water waves. In *Numerical Methods for Fluid Dynamics II*, pp. 671–679. Oxford University press.

FENG, T. & YANG, H. 2026 Solitary electrohydrodynamic waves with submerged point vortices. *J. Math. Fluid Mech.* **28** (2), 29.

GAO, T., WANG, Z. & PAPAGEORGIOU, D. 2024 Singularities of capillary-gravity waves on dielectric fluid under normal electric fields. *SIAM J. Appl. Maths* **84** (2), 523–542.

GRANDISON, S., PAPAGEORGIOU, D.T. & VANDEN-BROECK, J.-M. 2012 The influence of electric fields and surface tension on Kelvin–Helmholtz instability in two-dimensional jets. *Z. Angew. Math. Phys.* **63**, 125–144.

GRUE, J., FRIIS, H.A., PALM, E. & RUSAAS, P.O. 1997 A method for computing unsteady fully nonlinear interfacial waves. *J. Fluid Mech.* **351**, 223–252.

GUAN, X. & VANDEN-BROECK, J.-M. 2025 A time-dependent boundary-integral algorithm for nonlinear interfacial waves. *Comput. Fluids* **300**, 106739.

GUAN, X. & WANG, Z. 2022 Interfacial electrohydrodynamic solitary waves under horizontal electric fields. *J. Fluid Mech.* **940**, A15.

GUO, W., ZHANG, Q. & HE, D. 2023 On the nonlinear behaviour of the Rayleigh–Taylor instability with a tangential electric field for inviscid and perfect dielectric fluids. *J. Fluid Mech.* **958**, A36.

HOU, T.Y. & LI, R. 2007 Computing nearly singular solutions using pseudo-spectral methods. *J. Comput. Phys.* **226** (1), 379–397.

HOU, T.Y., LOWENGRUB, J.S. & SHELLEY, M.J. 1994 Removing the stiffness from interfacial flows with surface tension. *J. Comput. Phys.* **114** (2), 312–338.

HOU, T.Y., LOWENGRUB, J.S. & SHELLEY, M.J. 1997 The long-time motion of vortex sheets with surface tension. *Phys. Fluids* **9** (7), 1933–1954.

JACKSON, J.D. 2012 *Classical Electrodynamics*. John Wiley & Sons.

KOCHURIN, E.A. 2019*a* Formation of weak singularities on the surface of a dielectric fluid in a tangential electric field. *Tech. Phys. Lett.* **45**, 65–68.

KOCHURIN, E.A. 2019*b* Numerical simulation of the wave breaking process on the surface of a dielectric liquid in a tangential electric field. In *2019 IEEE 20th International Conference on Dielectric Liquids (ICDL)*, pp. 1–4. IEEE.

KOCHURIN, E.A. & ZUBAREV, N.M. 2018 Gravity-capillary waves on the free surface of a liquid dielectric in a tangential electric field. *IEEE Trans. Dielec. Elec. Insul.* **25** (5), 1723–1730.

KOCHURIN, E.A., ZUBAREV, N.M. & ZUBAREVA, O.V. 2013 Formation of curvature singularities on the interface between dielectric liquids in a strong vertical electric field. *Phys. Rev. E* **88** (2), 023014.

KRASNY, R. 1986*a* Desingularization of periodic vortex sheet roll-up. *J. Comput. Phys.* **65** (2), 292–313.

KRASNY, R. 1986*b* A study of singularity formation in a vortex sheet by the point-vortex approximation. *J. Fluid Mech.* **167**, 65–93.

LONGUET-HIGGINS, M.S. & COKELET, E. 1976 The deformation of steep surface waves on water-I. A numerical method of computation. *Proc. R. Soc. Lond. A* **350** (1660), 1–26.

MELCHER, J.R. & SCHWARZ JR., W.J. 1968 Interfacial relaxation overstability in a tangential electric field. *Phys. Fluids* **11** (12), 2604–2616.

MOORE, D.W. 1979 The spontaneous appearance of a singularity in the shape of an evolving vortex sheet. *Proc. R. Soc. Lond. A* **365** (1720), 105–119.

PAPAGEORGIOU, D.T. 2019 Film flows in the presence of electric fields. *Annu. Rev. Fluid Mech.* **51** (1), 155–187.

PULLIN, D.I. & SHEN, N. 2023 On vortex-sheet evolution beyond singularity formation. *J. Fluid Mech.* **976**, A17.

SOHN, S.-I. & BAEK, S. 2026 Suppression of Kelvin–Helmholtz instability by an electric field. *Phys. Fluids* **38** (1), 014108.

TILLEY, B.S., PETROPOULOS, P.G. & PAPAGEORGIOU, D.T. 2001 Dynamics and rupture of planar electrified liquid sheets. *Phys. Fluids* **13** (12), 3547–3563.

WANG, Z. 2017 Modelling nonlinear electrohydrodynamic surface waves over three-dimensional conducting fluids. *Proc. R. Soc. Lond. A* **473** (2200), 20160817.

https://doi.org/10.1017/jfm.2026.11860 Published online by Cambridge University Press

WANG, Z. 2022 Interfacial electrohydrodynamic waves under horizontal electric fields: Hamilton's principle and multi-scale modeling. *Adv. Mech.* **52** (3), 719–729.

WANG, Z. & MILEWSKI, P.A. 2012 Dynamics of gravity–capillary solitary waves in deep water. *J. Fluid Mech.* **708**, 480–501.

XU, G. & WANG, Z. 2025 Dynamics of solitary waves on a ferrofluid jet: the Hamiltonian framework. *J. Fluid Mech.* **1002**, A23.

YANG, Q., LI, B.Q., ZHAO, Z., SHAO, J. & XU, F. 2016 Numerical analysis of the Rayleigh–Taylor instability in an electric field. *J. Fluid Mech.* **792**, 397–434.

YANG, Y. 1992 The initial value problem of a rising bubble in a two-dimensional vertical channel. *Phys. Fluids* **4** (5), 913–920.

ZAKHAROV, V.E. 1968 Stability of periodic waves of finite amplitude on the surface of a deep fluid. *J. Appl. Mech. Tech. Phys.* **9** (2), 190–194.

https://doi.org/10.1017/jfm.2026.11860 Published online by Cambridge University Press